Problems in the technique of measuring signals by detectors without internal amplification

R. N. Krasnokutskiĭ, L. L. Kurchaninov, N. N. Fedyakin, and R. S. Shuvalov
Institute of High Energy Physics, Serpukhov

Fiz. Elem. Chastits At. Yadra **22**, 265–320 (January–February 1991)

The problems of increasing the accuracy of measuring the amplitude of signals from particle detectors without internal amplification are reviewed. The low level of the signals in such detectors imposes stringent constraints on the electronics noise, so that the preamplifier characteristics must be optimized for each particular detector and set of experimental conditions. The problems of amplitude measurements at large counting rates and also for galvanic, cable, and transformer detector–preamplifier couplings are discussed. It is shown that the use of time-variant signal filtration allows (a) improvement of the loading capability of the measuring section compared with time-invariant filtering and (b) attainment of a signal-to-noise ratio differing by 1.6% from the optimum.

INTRODUCTION

In recent decades new detectors have come into widespread use in high-energy physics. Examples of these are liquid-argon calorimeters, silicon microstrip and drift chambers, germanium 3-D detectors, Čerenkov and scintillation counters with photodiode (phototriode) readout, fast proportional chambers with low ($\geqslant 10^3$) amplification, time-projection gas and liquid-argon chambers, and high-pressure ionization gas calorimeters. A characteristic feature of all these detectors is the low signal level, and this requires the use of low-noise amplifiers. The preamplifier (PA) characteristics must be optimized for each individual detector and set of experimental conditions. In Table I, which is based on the data given in the reviews of Refs. 1 and 2, we give the characteristic signals of various detectors requiring low-noise PAs and the attainable noise levels for given experimental conditions: the detector capacitance and the loading capability (the characteristic signal duration). In this review the particle detectors themselves are hardly discussed at all, except in Sec. 3, where we describe the standard proportional chambers (PC) operating with low amplification coefficient and high speed. More detailed information on detectors and a bibliography can be found in the reviews of Refs. 1 and 2, and Ref. 3 discusses the status of the situation regarding the production and use of semiconductor particle detectors (SCD) in current experiments.

The diversity of detectors, experimental conditions, and parameters describing the measuring section makes it impossible to optimize the latter without an adequate computational model. In the present review we develop one and discuss it in considerable detail. In Sec. 1 we consider a charge-sensitive PA with slow (for amplitude measurement) and fast (for time measurements) outputs. Expressions are obtained for the signals at these outputs and for the spectral densities (SD) of the noise for arbitrary detector and feedback (FB) impedances. For capacitive–resistive FB the circuit that we analyze becomes the widely used charge-sensitive amplifier (CSA).

In Sec. 2 we propose a technique for selecting the head element of a PA operating at high counting rates. We also propose several practical PA circuits and give the experimental results of the operation of a fast PC. The higher loading capability of the chambers was obtained by using fast mixtures and low-noise PAs, which made it possible to work with a low gas amplification coefficient ($\geqslant 10^3$) and to avoid space-charge effects. Section 3 is devoted to the technique for calculating the equivalent noise charge (ENC) for time-variant (TV) signal filtering. The interest in TV filters has grown recently in connection with the design and preparation of experiments at current and future colliders: LEP, DESY, UNK, SSC, LHC, and so on. The enormous number of information channels in the central part of the setups at such colliders requires a high degree of electronics integration. Two versions of monolithic integrated circuits satisfying the requirements have already been developed on the basis of the MOS–VLSI technology.[4,5] In them the signal and noise filtering is performed not by ordinary amplifiers on *RC* chains, but by a combination which is easily realized with the existing technology: a MOS-switch and capacitance. Since the switch is controlled by an external trigger (as a rule, the time for the particles to intersect the collider is known), such a filter will be time-variant. In Sec. 3 we show that optimization of the measurement process makes it possible to realize the advantages of the TV filter over time-invariant ones. In Sec. 4 we study the problems arising in transformer coupling of the detector and PA, and we obtain expressions which make it possible to avoid the empirical selection of the large number of transformer parameters and reduce the optimization to the fulfillment of simple recipes. In Sec. 5 we calculate the effect of the information channels on each other owing to the presence of common impedances in the channel input circuits and also of inductive and capacitive coupling.

1. EQUIVALENT CIRCUIT FOR CALCULATING THE NOISE FOR GALVANIC DETECTOR–CSA COUPLING

In this section we calculate the CSA noise for arbitrary loading, feedback (FB), and detector impedances, which

TABLE I. Detectors using low-noise electronics.

Particle detector	Signal level	Detector capacity C_1, pF	Signal duration τ, μsec	Allowed e^- noise (rms)
Si-counter telescope	$7.5\cdot10^3$ e^-/100 μm	100-1000	0.03	2300
Ge detector (live target)	$18\cdot10^3$ e^-/100 μm	30	0.2	600
Si microstrip coordinate detector	$7.5\cdot10^3$ e^-/100 μm	30	0.03	1200
Total-absorption detector, interstratified with Si	272 e^-/keV	1000	2.0	$(1–5)\cdot10^3$
Time–projection gas chambers (TPC)	$5\cdot10^4$–10^5 e^-/removal element	5–10	0.25	500
High-pressure multilayer gas (Xe) ionization chamber	230 e^-/cm·atm	10^4	0.2	$1.8\cdot10^5$
BGO (photodiode removal)	10^3 e^-/MeV	100	2	500
Total-absorption Čerenkov counters with lead glass radiators (phototriode removal)	15 e^-/MeV	10	1.8	150
Liquid-argon calorimeter	$1.9\cdot10^4$ e^-/MeV	1000	2	$(1–5)\cdot10^3$

makes it possible to use the expressions obtained to analyze the noise of detectors with resistive information removal, for cable and transformer detector–amplifier coupling, and so on. For capacitive FB the circuit that we analyze becomes the widely used CSA, which has the same limiting resolution (ENC) as a voltage amplifier. The noise characteristics of the measuring section are studied in detail for cable detector–CSA coupling.

Driving characteristics of the noise and signal sources

We chose the circuit shown in Fig. 1a for analysis, since it represents a generalization of several familiar circuits. If the current in the load Z_3 is measured, we arrive at the circuit of Ref. 6; if the current at the output of the amplifier A is measured, we arrive at the circuit of Ref. 7; and if the voltage at the load Z_3 is measured, for $A = 1$ we arrive at the usual CSA (Ref. 8). We assume that the amplifier A has zero input and infinite output resistance and does not introduce additional noise. In Refs. 6 and 8–10 it was shown that for $A > 1$ the input resistance of the CSA (Fig. 1a) is decreased. This can prove useful if cable or transformer coupling between the detector and amplifier is used.

The noise spectral densities (SDs) (Fig. 1a) are

$$\overline{i_{1,2}^2}=2kT\frac{\mathrm{Re}(Z_{1,2})}{|Z_{1,2}|^2};\quad \overline{i_{\mathrm{ch}}^2}=2kTg_m, \tag{1}$$

where g_m is the transconductance of the field-effect transistor (FET).

We introduce the notation

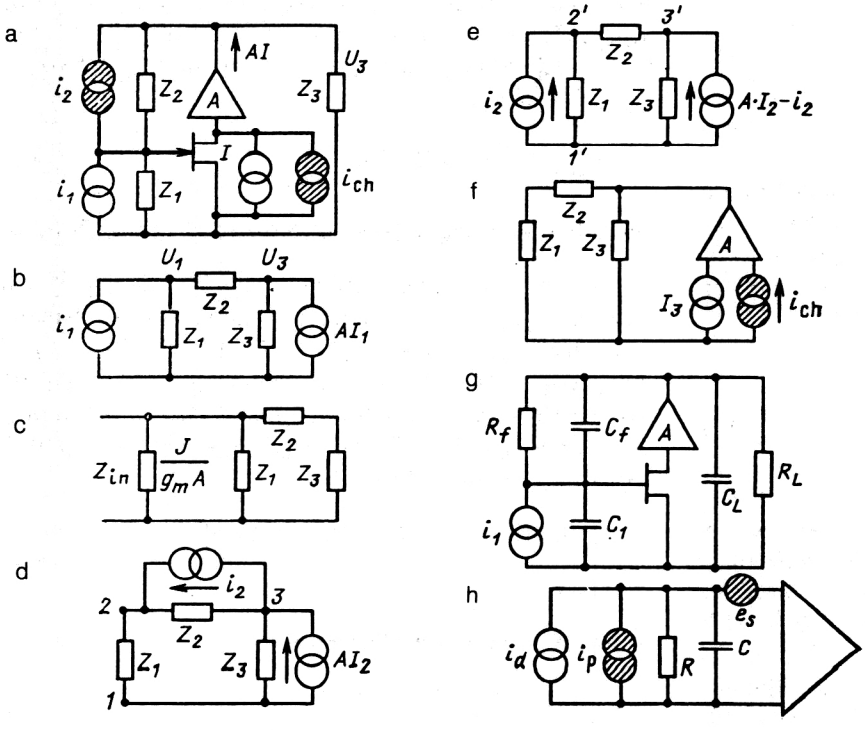

FIG. 1. Equivalent circuits for calculating noise and the detector signal at the CSA output.

$$I=-g_mU_1; \tag{2}$$

$$Z_0=Z_1+Z_2+Z_3. \tag{3}$$

Let us calculate the individual contributions of the sources of $i_{1,2}$ and i_{ch} to the voltage at the load Z_3 and the FET current I. Owing to the principle of superposition, the currents in the branches $Z_{1,2}$ are the sums of the currents from the sources AI and i_1 ($i_{2,ch}$ is neglected when the contribution from i_1 is calculated):

$$i_{Z_1}=\frac{U_1}{Z_1}=AI\frac{Z_3}{Z_0}+i_1\frac{Z_2+Z_3}{Z_0}; \tag{4}$$

$$i_{Z_3}=\frac{U_3}{Z_3}=AI\frac{Z_1+Z_2}{Z_0}+i_1\frac{Z_1}{Z_0}. \tag{5}$$

We use the expression for the current I(2) and substitute it into (4). The input impedance and admittance are

$$Z_{in}=\frac{U_1}{i_1}=\frac{Z_1(Z_2+Z_3)}{Z_0+Ag_mZ_1Z_3}; \tag{6}$$

$$Y_{in}=\frac{1}{Z_{in}}=\frac{1}{Z_1}+\frac{1}{Z_2+Z_3}+\frac{Ag_mZ_3}{Z_2+Z_3}. \tag{7}$$

We introduce the notation

$$J=(Z_2+Z_3)/Z_3. \tag{8}$$

The first two terms in (7) are the input admittance of the circuit in Fig. 1b, and the last reflects the effect of the generator of the current AI. As can be seen from (7), it reduces to connecting an additional impedance $J(Ag_m)^{-1}$ in parallel with the input (Fig. 1c).

Transforming (4), we find the transfer functions of the generator of i_1 in the current and voltage, respectively:

$$G_1(p)=AI_1/i_1=-Z_{in}Ag_m; \tag{9}$$

$$H_1(p)=\frac{U_3}{i_1}=\frac{Z_{in}}{J}Z_2\left(\frac{1}{Z_2}-Ag_m\right). \tag{10}$$

The contribution of the noise source i_2, coupled to the active component of the FB impedance Z_2, to the voltage U_3 and current AI_2 at the CSA output is calculated from the circuit of Fig. 1d. The final expressions for the transfer functions in the voltage and current are

$$H_2(p)=U_3/i_1=-Z_{in}Z_2A(Z_1^{-1}+Ag_m)/J;$$
$$G_2'(p)=\frac{AI_2}{i_2}=-\frac{Z_1Z_2Ag_m}{Z_0+Z_1Z_3Ag_m}. \tag{11}$$

In practical circuits one measures not AI_2, but the total current flowing through the node 3 to the impedances $Z_{2,3}$, or the portion of it flowing to Z_3, and therefore for the rest of the analysis we will use the circuit of Fig. 1e. It is easily verified that the currents flowing to the nodes 1, 2, 3 of the circuit in Fig. 1d are the same as those flowing to the nodes 1′, 2′, 3′ of the circuit of Fig. 1e, and therefore the two circuits are equivalent. The latter redefines the transfer function in the current:

$$G_2(p)=\frac{AI_2-i_2}{i_2}=\frac{Z_0+Z_1(Z_2+Z_3)Ag_m}{Z_0+Z_1Z_3Ag_m}. \tag{12}$$

We determine the transfer function of the thermal-noise generator of the channel using the circuit of Fig. 1f. The presence of an additional source of noise I_3 (it is introduced in Ref. 6 without explanation) arises from the fact that the channel noise current i_{ch} affects the gate through the FB loop, and the voltage at the gate is transformed into an additional current. Therefore, the total transfer characteristic in the current can be written as

$$G_3(p)=\frac{A(I_3+i_{ch})}{i_{ch}}. \tag{13}$$

The current I_3 and the voltage U_3 at the load Z_3 are related as

$$I_3=-U_1g_m=-U_3g_mZ_1(Z_1+Z_2)^{-1}; \tag{14}$$

$$U_3=A(I_3+i_{ch})Z_3(Z_1+Z_2)Z_0^{-1}. \tag{15}$$

From (14) and (15) we find

$$I_3+i_{ch}=-I_3Z_0(Z_1Z_3g_mA)^{-1}. \tag{16}$$

Expressing I_3 in terms of i_{ch} and substituting the result into (13), we obtain, taking into account (6),

$$G_3(p)=AZ_{in}[(Z_2+Z_3)^{-1}+Z_1^{-1}]. \tag{17}$$

We substitute into (17) the value of Z_{in} and transform it:

$$G_3(p)=\frac{AZ_0}{Z_0+Z_1Z_3Ag_m}=A\left(1-\frac{g_mZ_1Z_3}{Z_0+Z_1Z_3Ag_m}\right). \tag{18}$$

The second term in parentheses can vary from 0 ($Z_0 \gg g_mZ_1Z_3A$) to 1 ($Z_0 \ll g_mZ_1Z_3A$). Substituting (14) into (15), we find the transfer characteristic of the generator of i_{ch} in the voltage:

$$H_3(p)=\frac{U_3}{i_{ch}}=A\frac{Z_{in}}{J}\left(1+\frac{Z_2}{Z_1}\right). \tag{19}$$

Detector with capacitive impedance at the CSA input

Here we show that when analyzing noise the CSA can be replaced by a voltage amplifier, and we can calculate the equivalent noise charge (ENC) of the CSA for optimal filtering and for a detector with finite signal duration. We assume that the detector has a purely capacitive impedance, and that the FB and load loops have capacitive–risistive impedance (Fig. 1g):

$$Z_1=(pC_1)^{-1};\quad Z_2=[C_f(p+\omega_f)]^{-1};$$
$$Z_3=[C_L(p+\omega_L)]^{-1}. \tag{20}$$

Then (8) can be transformed to

$$J=\frac{Z_1+Z_2}{Z_3}=\frac{C_L+C_fp+\omega_{z.p.c.}}{C_f}\frac{}{p+\omega_f}. \tag{21}$$

In Eqs. (20) and (21) we use the notation

$$\omega_f^{-1}=R_fC_f;\quad \omega_L^{-1}=R_LC_L;$$

$$\omega_{\text{z.p.c.}}^{-1}=R_L\|R_f(C_L+C_f).$$

When the condition $\omega_L = \omega_f = \omega_{\text{z.p.c.}}$ (z.p.c. stands for zero–pole cancellation) is satisfied, the pole is canceled by the zero and J is independent of the frequency:

$$J=(C_L+C_f)/C_f=C_0/C_f. \tag{22}$$

We carry out the rest of the calculations assuming that the conditions for zero–pole cancellation are satisfied.

We find the expression for the input admittance:

$$Y_{\text{in}}=Z_{\text{in}}^{-1}=pC_1+C_L(p+\omega_{\text{z.p.c.}})/J+Ag_m/J. \tag{23}$$

We substitute into (23) the expression for $\omega_{\text{z.p.c.}}$ and use the fact that in practical circuits $R_L \sim 10^6\ \Omega$ and $g_m^{-1} \sim 100\ \Omega$, so that $(JR_L)^{-1} \ll Ag_m/J$. We obtain

$$Y_{\text{in}}=Z_{\text{in}}^{-1}=C_{\text{in}}(p+\alpha_{\text{in}}), \tag{24}$$

where $C_{\text{in}} = C_1 + C_L/J \approx C_1 + C_f$ is the reactive component of the CSA impedance and $\alpha_{\text{in}}^{-1} = (C_{\text{in}}R_{\text{in}})$ is the time constant of the input loop.

The active component of the input impedance of the CSA is independent of frequency and equal to

$$R_{\text{in}}=J/(Ag_m)=C_0/(C_fAg_m). \tag{25}$$

The response of the input loop to a signal in the form of a current δ function is

$$U_{\text{in}}(t)=C_{\text{in}}^{-1}\exp(-\alpha_{\text{in}}t).$$

According to (8), the output current of the FET has the same form:

$$i(t)=-Ag_m/C_{\text{in}}\exp(-\alpha_{\text{in}}t). \tag{26}$$

Using the expression for the input impedance (24), we rewrite the transfer characteristic $G_1(p)$ as

$$G_1(p)=-Z_{\text{in}}Ag_m=-J\alpha_{\text{in}}/(p+\alpha_{\text{in}}), \tag{27}$$

from which we see that J actually determines the current amplification.

The voltage at the load Z_3 can be found from (9). We simplify the expression in parentheses:

$$C_f(p+\omega_f)-Ag_m \approx -Ag_m$$

and neglect frequencies larger than $Ag_m/C_f \approx 10^{11}\ \text{sec}^{-1}$. Then the expression for the transfer function in the voltage of the source of t_1 takes the form

$$H_1(p)=-\frac{\alpha_{\text{in}}}{C_f}\frac{1}{(p+\alpha_{\text{in}})(p+\omega_f)}, \tag{28}$$

i.e., the input voltage pulse grows with the time constant of the input loop α_{in}^{-1} and falls slowly with the time constant ω_f^{-1}. Using the fact that $C_{\text{in}} = C_1 + C_L/J \approx C_1$ and introducing the constant $\lambda = Ag_mC_1^{-1}$, we rewrite the expressions for the transfer functions of the noise source i_2 of the FB resistor R_f in the current and the voltage as

$$G_2(p)=-\frac{p+\lambda}{p+\alpha_{\text{in}}}; \tag{29}$$

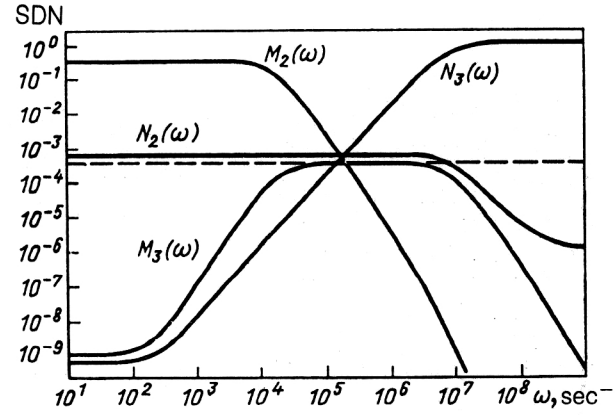

FIG. 2. Spectral densities of noise (SDN) at the current output of a CSA, $N_{2,3}(\omega)$, and at the charge output, $M_{2,3}(\omega)$.

$$H_2(p)=-\frac{1}{C_f}\frac{p+\lambda}{p+\alpha_{\text{in}}}\frac{1}{p+\omega_f}. \tag{30}$$

The transfer characteristics of the generator of i_{ch}—the source of thermal noise in the FET channel—is found in a similar manner:

$$G_3(p)=A\frac{p+\omega_1}{p+\alpha_{\text{in}}}; \tag{31}$$

$$H_3(p)=\frac{A}{C_0}\frac{p+\omega_1}{p+\alpha_{\text{in}}}\frac{1}{p+\omega_f}. \tag{32}$$

The noise spectral densities (SDs) of the generators of i_2 and i_{ch} at the CSA output can be written in the following form using the Carson theorem:

$$\left.\begin{aligned} N_2(\omega)&=2kTR_f^{-1}|G_2(\omega)|^2;\\ M_2(\omega)&=2kTR_f^{-1}|H_2(\omega)|^2;\\ N_3(\omega)&=2kTg_m|G_3(\omega)|^2;\\ M_3(\omega)&=2kTg_m|H_3(\omega)|^2, \end{aligned}\right\} \tag{33}$$

where $G_{2,3}$ and $H_{2,3}$ are given by Eqs. (29)–(32) if the Laplace variable in them is replaced by $j\omega$. Since the noise sources i_2 and i_{ch} are independent, the total SDs of the noise in the current and the voltage at the CSA output are equal to the sum of their components:

$$\left.\begin{aligned} N(\omega)&=N_2(\omega)+N_3(\omega);\\ M(\omega)&=M_2(\omega)+M_3(\omega). \end{aligned}\right\} \tag{34}$$

Comparison of (27) and (29) shows that for frequencies $\omega \ll \lambda$ the transfer characteristics of i_1 and i_2 coincide, which is also observed in the voltage amplifier (Fig. 1h).

In Fig. 2 we give the noise SDs of the output currents $[N_{2,3}(\omega)]$ and voltages $[M_{2,3}(\omega)]$ calculated using Eqs. (33). For convenience the curves in the same figure are orthonormalized in an arbitrary fashion. The values of the CSA and detector parameters are

$C_{\text{in}}=20$ pF; $g_m=20$ mA/V;

$R_f=47$ MΩ; $C_f=1.1$ pF.

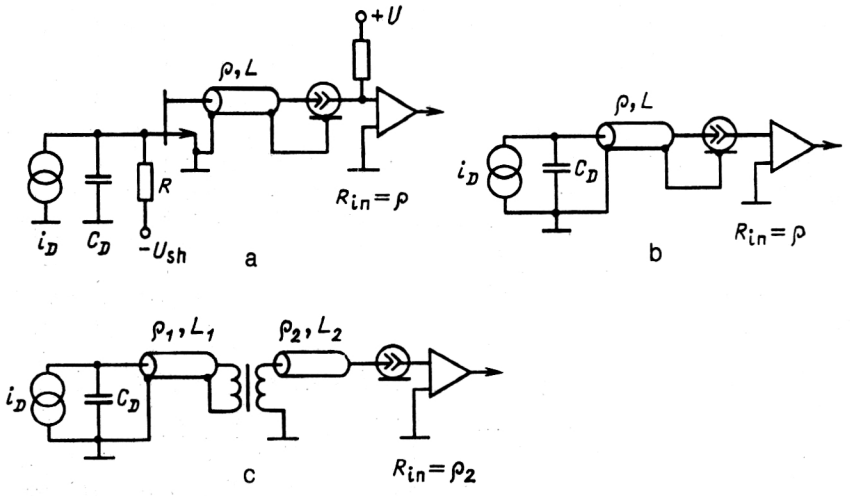

FIG. 3. Three ways of connecting a detector and an amplifier using a long line.

We shall now show that if the voltage at the CSA output is measured, then in the noise analysis the CSA can be replaced by a voltage amplifier (Fig. 1h). Since $M_2(\omega) > M_3(\omega)$, at frequencies $\omega < \omega_c$ [where ω_c is the frequency at which the noise SDs are compared, $M_2(\omega_c) = M_3(\omega)$] it is possible to take $M_3 = \text{const}$ in this frequency range without noticeable error. At high frequencies it is also possible to take $M_3 = \text{const}$, since for the optimal separation of the signal from the noise it is necessary anyhow to filter out all frequencies beyond the frequency spectrum of the signal. However, assuming that the channel noise is white (dashed line in Fig. 2), we immediately arrive at the circuit for an ideal voltage amplifier. To simplify the analysis it is common to take $\omega_{\text{z.p.c.}} = \omega_L = \omega_f$, i.e., to replace the exponential signal by a step, and the parallel noise (i_2) by a θ-function current. We see from Fig. 2 that this simplification also does not lead to error, since the noise SD and the squared modulus of the Fourier transform of the signal (i_1) have the same shape and transform identically under the "whitening" operation: in the time region the signal will have an exponential form with time constant ω_c^{-1}, and the parallel noise is transformed into a Poisson current of such exponentials. As was shown in Ref. 11, the ENC for optimal filtering of the signal after the CSA (a δ function at the detector output) is

$$\text{ENC}_{\text{opt}}^2 = 4kT\frac{C_1}{g_m}\left|\frac{g_m}{R_f}\right|^{1/2}, \tag{35}$$

which coincides with the widely known result for a voltage amplifier[12] (i.e., without feedback; Fig. 1h).

If the detector signal is an exponential with time constant ε^{-1},

$$s(t) = \varepsilon \exp(-\varepsilon t), \tag{36}$$

then the maximum energy resolution will be worse:[11]

$$\text{ENC}_{\text{opt}}^2(\varepsilon) = 4kT\frac{C_1}{g_m}\left|\frac{g_m}{R_f}\right|^{1/2}\left\{1+\frac{\omega_c}{\varepsilon}\right\}. \tag{37}$$

We see from this equation that even for optimal filtering the finite signal duration introduces an appreciable contribution to the energy resolution of "slow" detectors without internal amplification, such as liquid-argon detectors and scintillation detectors with photodiode readout based on BGO, NaI(Tl), CsI(Tl), and other calorimeters.

Connecting a detector and a CSA by means of a long line

Owing to the large geometrical dimensions of present and future particle detectors in high-energy physics, it is necessary to use one of the following methods to connect a detector and a preamplifier (CSA) (Fig. 3). In the circuit of Fig. 3a the head element (usually a FET) is monitored directly at the electrodes and connected to the main amplifier by a long band line or a cable. This has an obvious deficiency: the entire detector must be disassembled for output from the structure of the head element, which is especially difficult for the 4π geometry of detectors in colliding beams or large liquid-argon calorimeters. In the variant of Fig. 3b the cable capacitance is connected directly to the CSA input in parallel with the detector capacitance, which worsens the signal-to-noise ratio. In the circuit of Fig. 3c the signal-to-noise ratio is improved by use of a transformer. This variant cannot be used when operating in strong magnetic fields, owing to ferrite saturation. If the signal duration at the output of the shaping amplifier is much larger than the time for the signal to travel along the cable, then the noise characteristics can be calculated by replacing the cable with a localized capacitance without leading to large error. However, the requirements on detector operating speeds are constantly becoming more demanding, and for certain relations between C_d, l, and the shaping time τ the replacement of the cable by a localized capacitance can lead to large errors in the signal-to-noise calculations. Let us consider the transport of a detector signal (a current δ function of amplitude I_d) to the input of a CSA with capacitive–resistive feedback and load (Fig.

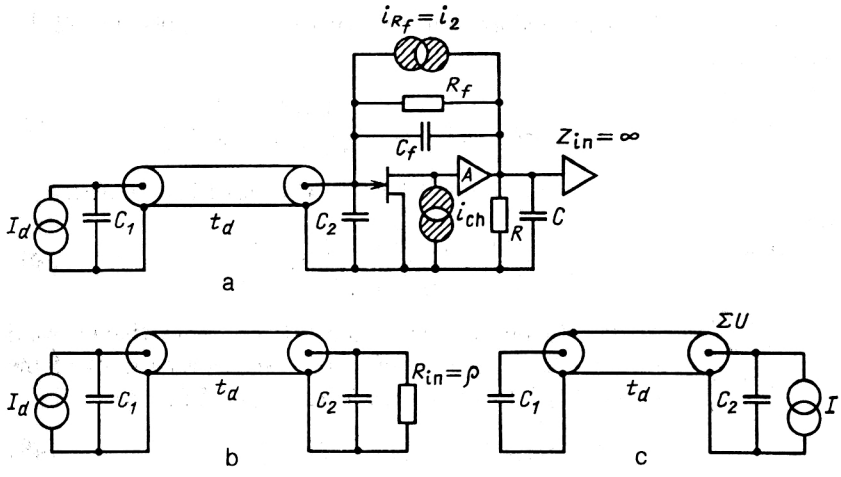

FIG. 4. Equivalent circuits for calculating the noise in signal transfer via a cable from the detector with C_1 to a CSA with "cold" resistance: (a) complete circuit with all signal and noise sources; (b) simplified circuit for calculating the signal at the CSA output; (c) circuit for calculating the impedance of a cable loaded with $C_{1,2}$.

4a). In this case the input impedance is purely active and is given by Eq. (25). To analyze the passage of the signal through the cable we use the simplified circuit shown in Fig. 4b. The input resistance is assumed to be equal to the wave resistance of the cable, $R_{in} = \rho$. We introduce the notation

$$t_1=\rho C_1, \quad t_2=\rho C_2,$$

where $C_{1,2}$ are the detector and CSA capacitances, respectively.

The Laplace transformation of the voltage at the CSA input will be

$$U_1(p)=\frac{I_d\rho}{1+pC_1\rho}\exp(-pt_d), \tag{38}$$

where t_d is the time for the signal to travel along the cable.

The presence of the capacitance C_2 at the CSA input will cause reflection of the signal because the impedance matching of the long line and the load is spoiled. Multiple reflections are taken into account by adding new terms of the form

$$U_{1n}=\left[\frac{1-pt_1}{1+pt_1}\frac{-pt_2}{2+pt_2}\right]^{n-1}\frac{2I_d\rho e^{-(1+2n)pt_d}}{(1+pt_1)(2+pt_2)}. \tag{39}$$

In Fig. 5 we show the calculated pulse shapes at the current output of the CSA after a 50 Ω cable, taking into account multiple reflections from the CSA input. The detector capacitance was taken to be $C_1 = 400$ pF, and the input capacitance of the CSA was $C_2 = 200$ pF (the SNJ 3600 and NJ 903L transistors have input capacitances $C_2 = 150$ pF and $C_2 = 600$ pF, respectively, for a current $I_d = 20$ mA; Ref. 13). As can be seen from Fig. 5, the contribution of multiple reflections related to the presence of a large input capacitance becomes smaller, the longer the duration of the detector signal compared with the time

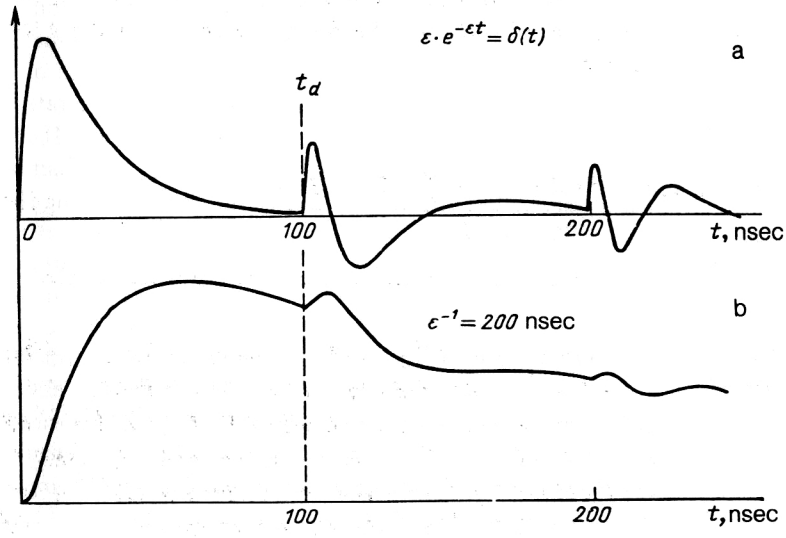

FIG. 5. Shapes of pulses at the current output of the CSA, distorted by multiple reflections from the ends of a long line: (a) δ-function detector signal; (b) detector signal which is an exponential with time constant $\varepsilon^{-1} = 200$ nsec.

for the signal to propagate along the cable. When the cable impedance coincides exactly with the input impedance of the amplifier (when C_2 can be neglected), there are no secondary reflections, and the voltage generated by the signal will be given by (38).

To calculate the transfer characteristics of the noise it is necessary to reduce the circuit of Fig. 4a to the form in Fig. 1a, where Z_1 is the impedance of the cable loaded at its two ends with capacitances $C_{1,2}$, and then use Eqs. (12) and (17). We shall calculate the impedance of a cable with capacitive loads $C_{1,2}$ as the ratio of the voltage across the capacitance C_2, generated by a given source of current I connected in parallel with C_2, to the value of I. The initial value of the voltage across C_2 is

$$U_1=\frac{I\rho}{1+pt_2}. \tag{40}$$

After reflection of the signal from the detector capacitance across C_2 with delay $2t_d$ we obtain the addition

$$U_2=\frac{1-pt_1}{pt_1+1}\frac{2}{pt_2+1}U_1e^{-2t_dp}. \tag{41}$$

Each reflection from the loads C_1 and C_2 gives the factors

$$\gamma_{1,2}=(1-pt_{1,2})(1+pt_{1,2})^{-1}. \tag{42}$$

The problem therefore reduces to the summation of the terms

$$U_n=\gamma_1^{n-1}\gamma_2^{n-2}\frac{2I_d\rho}{(1+pt_2)^2}e^{-2(n-1)t_dp},\quad n\geqslant 2, \tag{43}$$

with the expressions (40) and (41). The total voltage generated, taking into account all reflections, can be written as

$$\sum U=\left\{\frac{I\rho}{1+pt_2}+\frac{\gamma_1}{(1+pt_2)^2}\frac{2I\rho\exp(-2t_dp)}{1-\gamma_1\gamma_2\exp(-2t_dp)}\right\}. \tag{44}$$

The impedance of a cable loaded with capacitances $C_{1,2}$ is expressed as

$$Z_1=\frac{\sum U}{I}=\frac{\rho[1+\gamma_1\exp(-2t_dp)]}{(1+pt_2)[1-\gamma_1\gamma_2\exp(-2t_dp)]}. \tag{45}$$

Let us transform Eq. (6) for the input impedance of the CSA:

$$Z_{\text{in}}^{-1}=\frac{1}{Z_1}+\frac{1}{Z_2+Z_3}+\frac{Ag_mZ_3}{Z_2+Z_3}\cong\frac{1}{Z_1}+\frac{1}{\rho}. \tag{46}$$

After the substitution of (45) into (46) we obtain

$$Z_{\text{in}}=\frac{\rho[1+\gamma_1\exp(-2t_dp)]}{2+pt_2+pt_2\gamma_1\exp(-2t_dp)}. \tag{47}$$

In what follows we shall assume that $t_2=0$ (which is valid in the case $C_1\gg C_2$) and shall neglect reflections of the signal from the CSA side. Then (47) simplifies:

$$Z_{\text{in}}=0.5\rho[1+\gamma_1\exp(-2t_dp)]. \tag{48}$$

The SD of the channel noise i_{ch} can be written as

$$S_{\text{ch}}(\omega)=G_3(j\omega)G_3(-j\omega)i_{\text{ch}}^2\quad(-\infty<\omega<+\infty), \tag{49}$$

where $i_{\text{ch}}^2=2kTg_m$, and the expression for G_3 is

$$G_3(p)=AZ_{\text{in}}Z_1^{-1}=0.5A[1-\gamma_1\exp(-2t_dp)]. \tag{50}$$

We substitute (50) into (49) and obtain

$$S_{\text{ch}}(\omega)=2kTg_mA^2\frac{1+t_1^2\omega^2+\text{cw}(t_1^2\omega^2-1)+2\text{sw}t_1\omega}{1+t_1^2\omega^2}, \tag{51}$$

where we have introduced the notation $\text{cw}=\cos(2t_d\omega)$, $\text{sw}=\sin(2t_d\omega)$.

The transfer characteristic $G_2(p)$ (12) of the source of current I_2 related to the feedback-resistor noise can be rewritten as

$$G_2(p)=1+\frac{Z_1Z_2Ag_m}{Z_0+Z_1Z_3Ag_m}=\frac{J_1+\gamma_1J_2\exp(-2t_dp)}{2}. \tag{52}$$

We introduce the notation

$$J_1=J+1,\quad J_2=J-1;$$

$$J_3=J^2+1;\quad J_4=J^2-1.$$

Taking into account the fact that $i_2^2=2kT/R_f$, we obtain an expression for the noise SD scaled to the CSA output:

$$S_2(\omega)=2kT/R_f[G_2(j\omega)G_2(-j\omega)]=2kT/R_f\frac{(t_1^2\omega^2+1)J_3+\text{cw}\,J_4(1-t_1^2\omega^2)-2\text{sw}J_4T_1\omega}{2(1+t_1^2\omega^2)}. \tag{53}$$

In Fig. 6 we show the noise SD dependences S_{ch} and S_2 on the frequency for the following CSA and cable parameters:

$A=1$; $g_m=20$ mA/V; $R_f=4.7$ MΩ;

$C_1=1$ nF; $\rho=150$ Ω; $l=10$ m.

The dashed line in Fig. 6 shows the noise SD of a CSA loaded with a localized impedance. The calculated dependences of the equivalent noise charge ENC (FWHM)[1)] on C_{tot}, where $C_{\text{tot}}=C_1+C_c$ (C_c is the cable capacitance) are shown in Fig. 7 for various shapings of an $(RC)^2$ noise-reduction filter. The CSA parameters are the same, and

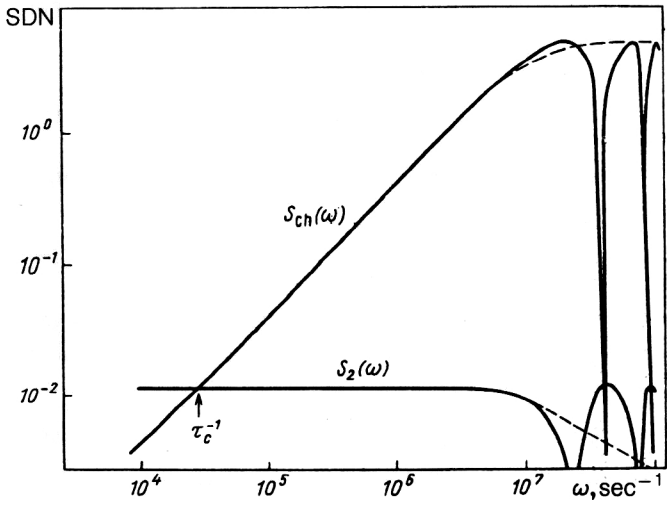

FIG. 6. SD of noise at the current output of a CSA when the detector is connected to the amplifier via a cable.

$C_1 = 100$ pF, $\rho = 50\ \Omega$. It can be seen that: (1) the dependence ENC(C_1) in the case of a localized capacitance is linear; (2) the dependence ENC(C_{tot}) differs significantly from a linear dependence; (3) for large cable lengths ENC(C_{tot}) enters a plateau. The authors of Ref. 14 have studied the influence of cable detector–CSA coupling on the noise characteristics of the measuring section and give the experimental dependence of ENC(C_{tot}) for an amplifier assembled from bipolar transistors. The results obtained experimentally confirm the calculated noise characteristics shown in Fig. 7.

2. ELECTRONICS FOR HIGH-SPEED DETECTORS

At high counting rates ($> 10^5$ pulse/sec) a preamplifier based on bipolar transistors (BT) has a larger signal-to-noise ratio than one based on a FET (Ref. 15). In this section we study the noise characteristics of BTs and give four circuits for low-noise preamplifiers.

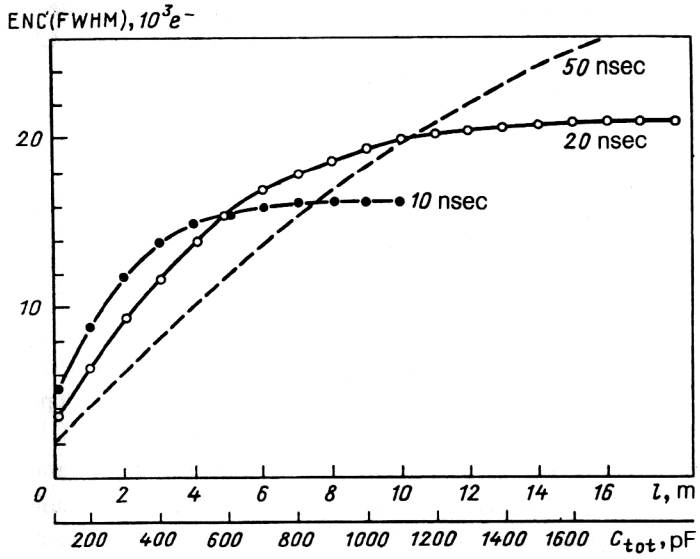

FIG. 7. The dependence ENC(C_{tot}), where $C_{tot} = C_1 + C_c$ (the cable capacitance C_c is varied) for various durations of an $(RC)^2$ noise-reduction filter (numbers near the curves). Parameters used in the calculations: $C_1 = 100$ pF, $q_m = 20$ mA/V, $R_f = 4.7$ MΩ, $\rho = 50\ \Omega$.

Equivalent noise charge of a bipolar transistor

The equivalent circuit for a noisy BT is shown in Fig. 8a. The three sources of noise have the spectral densities

$$\frac{d}{df}\overline{e_{BB'}^2} = 4kTr_{BB'}; \tag{54}$$

$$\frac{d}{df}\overline{i_B^2} = 2qI_B; \tag{55}$$

$$\frac{d}{df}\overline{i_c^2} = 2qI_c, \tag{56}$$

where I_B and I_c are the base and collector currents, and q is the electron charge. Rescaling of the noise SD to the output (the collector) gives[15]

$$N(\omega) = 2qI_c \left\{1 + \frac{C_D^2}{(C_D + C_B)^2}\frac{\omega^2\tau_0^2 2g_m r_{BB'}}{(1+\omega^2\tau_0^2)} + \frac{\beta^2}{B}\frac{1}{1+\omega^2\tau_0^2}\right\}, \tag{57}$$

where C_D is the detector capacitance, C_B is the intrinsic capacitance of the BT,

$$g_m = qI_c/(kT) \tag{58}$$

is the transconductance of the BT, and

$$B = I_c/I_B, \quad \beta = dI_c/dI_B; \tag{59}$$

$$\tau_0 = \beta g_m^{-1}(C_D + C_B). \tag{60}$$

Expression (57) can be used to calculate the ENC of the BT:

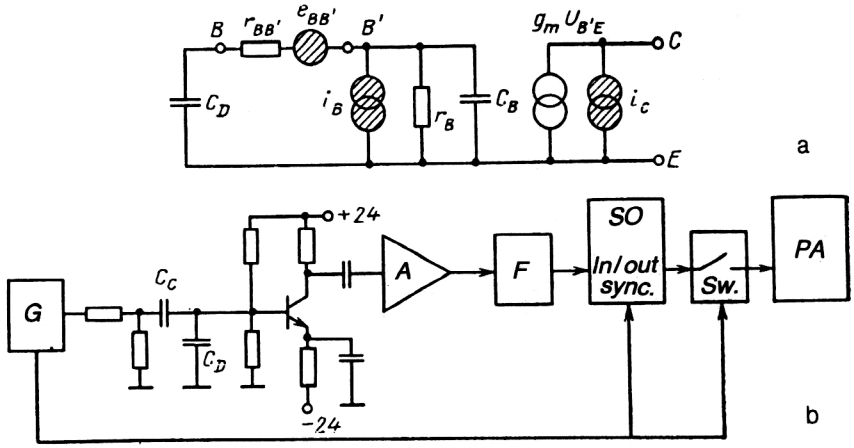

FIG. 8. (a) Equivalent circuit of a noisy BT and (b) circuit for measuring the ENC.

$$\text{ENC(FWHM)} = 2.35 \frac{\left[2\pi \int_{-\infty}^{+\infty} N(\omega)|F(\omega)|^2 \, d\omega\right]^{1/2}}{\left[\int_{-\infty}^{+\infty} \exp(jt\omega) S(\omega) F(\omega) \, d\omega\right]_{t_{\max}}}, \quad (61)$$

where $S(\omega)$ is the frequency transfer characteristic of the signal at the BT output and $F(\omega)$ is the frequency characteristic of the filter following the BT.

The ENC measurements were made using the circuit of Fig. 8b. The square-wave generator G has a front of $\leqslant 5$ nsec, so that the BT input receives a current pulse having the form of a δ function:

$$i_D(t) = Q\delta(t). \quad (62)$$

If U_G is the amplitude of the signal from the generator, then

$$Q = C_c U_G. \quad (63)$$

The capacitance C_D mimics the detector capacitance. A shaper of the *RC–CR* type with equal integration and differentiation times τ is used as the filter F. A stroboscope oscillograph (SO) is an ideal peak detector.[16]

The dependence of the ENC on C_D, τ, and I_c was measured for various types of BT. The best were KT382 (Ref. 17), KT391, KT399, KT640, KT3124 (Ref. 18), and KT396 (Ref. 19). In Fig. 9 the dots show the results of the ENC measurements for the KT640 transistor for $I_c = 0.3$ mA and $\tau = 20$, 50, and 100 nsec. The solid lines are the results of the calculations using (61). We see that the calculation agrees with the measurements to within 10–15%. The good agreement makes it possible to study the dependence of the ENC on the transistor parameters (β,$r_{BB'}$,f_T,I_c) and the measurement conditions (τ,C_D) without making difficult measurements.

A detailed analysis was carried out in Ref. 17 and shows that:

1. There exists an optimal τ which increases with decreasing I_c.

2. For fixed τ there is an optimal current I_c, which decreases with increasing τ.

3. With increasing β the dependence ENC(C_D) is

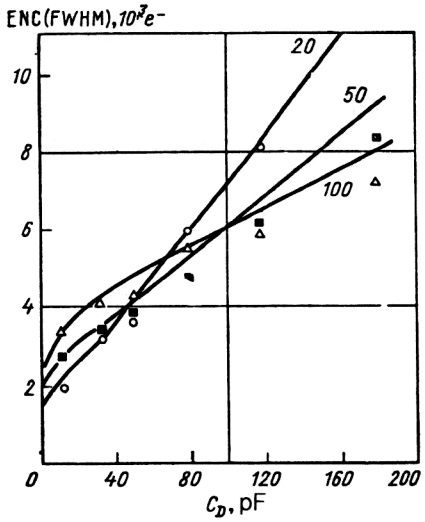

FIG. 9. Dependence of the ENC on the detector capacitance for the KT640 transistor for $I_c = 0.3$ mA. The points are the measurement results, and the curves were calculated using Eq. (8); the numbers near the curves are the values of τ in nsec.

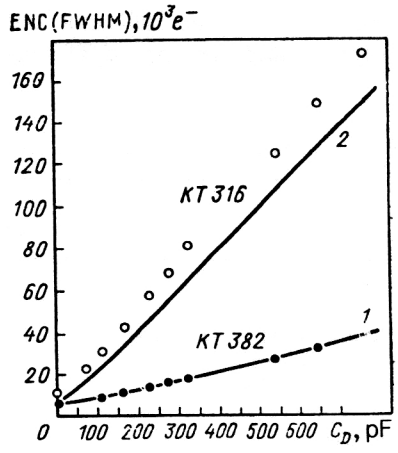

FIG. 10. Dependence of the ENC on the detector capacitance for transistors of the type KT316 ($r_{BB'} = 300\ \Omega$) and KT382 ($r_{BB'} = 30\ \Omega$).

TABLE II. Characteristics of domestically manufactured bipolar transistors.

Type of BT	Polarity	f_T, GHz	β	$r_{BB'}$, Ω
KT368	$n-p-n$	0,9	90—150	20—35
KT382	$n-p-n$	1,8	100—220	25—45
KT391	$n-p-n$	6,0	50—130	15—30
KT399	$n-p-n$	1,8	85—110	5—9
KT3124	$n-p-n$	6,0	60—150	14—36
KT3132	$n-p-n$	5,6	100—160	14—20
KT640	$n-p-n$	4,0	50—170	5—11
KT3109	$p-n-p$	0,8	40—100	10—30
KT3127	$p-n-p$	0,6	30—75	20—30
KT396	$n-p-n$	2,8	150—210	7—15
KT3121	$n-p-n$	2,5	40—60	8—16
KT629	$p-n-p$	—	40—70	3,5—5

shifted downward without change of the slope.

4. Decrease of the maximum frequency f_T from 3 to 0.3 GHz noticeably increases the ENC only for small C_D < 10 pF.

5. The slope of the dependence ENC(C_D) increases with increasing $r_{BB'}$. Here the value of the ENC for C_D = 0 is not changed.

In Fig. 10 we show the dependences ENC(C_D) for $\tau = 20$ nsec for the KT382 ($r_{BB'}$ = 30 Ω, curve 1) and KT316 ($r_{BB'}$ = 300 Ω, curve 2) transistors. We see that the choice of a head element with a small value of $r_{BB'}$ is important.

Unfortunately, the handbook data do not permit $r_{BB'}$ to be determined. The methods of measuring the distributed resistance of the base recommended in the literature[20,21] are either too awkward or require special apparatus which is usually not available in nuclear-physics laboratories. For the mass production of low-noise amplifiers it is necessary to discard the transistors, since the method of measuring $r_{BB'}$ must be simple. In Ref. 15 we suggested a method satisfying this condition. It is based on measurement of the noise SD/BT at a fixed frequency with incorporation of the BT using a circuit with a common emitter.

We used this method to measure $r_{BB'}$ for 43 types of domestically manufactured BT of the hf and uhf ranges.[15,19,22,23] As a result, we found the types of BT suitable for use as the head element of a low-noise preamplifier (Table II). The values of f_T are the handbook values.[24]

In practice, the best results were obtained with BTs of the types NEO21, NE578, NE734, and BFT25 (Refs. 25 and 26). Reference 27 gives the results of measurements and calculations of the ENC for the transistors NEO21, NE635, NE645, and NE681. Comparison with domestically manufactured transistors shows that the KT640 has an ENC as good as that of the best Japanese transistors.

Low-noise amplifiers based on bipolar transistors

Of the published circuits for low-noise preamplifiers (PA) based on BTs, that based on the CE–CC (the first transistor incorporated via a circuit with a common emitter, and the second via one with a common collector) circuit[28] is noteworthy for its simplicity and technical characteristics. However, to obtain a high operating speed this circuit requires that a transistor with very small collector–base capacitance be used as the head element, which is not always possible. It seems to us that the CE–CB (cascade) configuration, which is in addition distinguished by high stability and lack of sensitivity to the circuit board, is more suitable.

We constructed three PAs based on this configuration; their parameters are given in Table III, and their circuits in Figs. 11–13.

TABLE III. Parameters of low-noise amplifiers which have been designed.

Amplifier circuit Technology	Fig. 11 (Ref. 29) Thin-film	Fig. 12 (Ref. 30) "RITM"	Fig. 13 (Ref. 31) Discrete
Number of channels on the substrate	11	4	16
Substrate area, mm^2	40×60	20×50	120×80
Duration of output pulse at a level of 0.1 of the amplitude, nsec	70	20	15
Rise time (from a level of 0.1 to 0.9), nsec	···	4	4
Conversion coefficient for $C_D = 0$, μV/electron	0.086	0.50	1.0
ENC (FWHM) for $C_D = 0$, 10^3 e^-	4–5	3–4	2.5–3
Required power of one channel, mW	80	90	110
Input resistance, Ω	380	150	100
Pickup at a neighboring channel	2%	0.6%	···

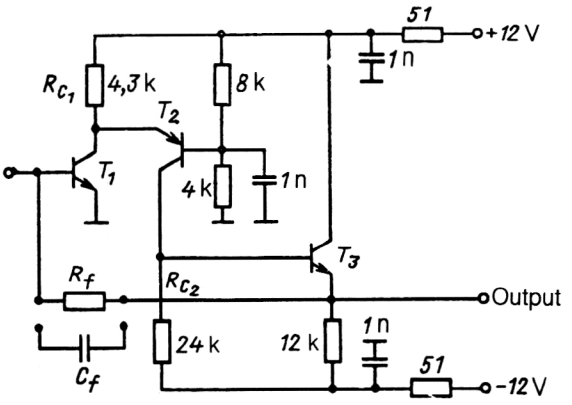

FIG. 11. Schematic diagram of a hybrid preamplifier: T_1, T_2, T_3 are KT384, KT370, and KT354, respectively. The feedback capacitance C_f is external, and $R_f = 25\ \text{k}\Omega$.

The listed preamplifiers are suitable for use with any small-capacitance detectors, but the electronics channel of a high-speed gas detector must contain an amplifier–shaper in which networks suppressing the hyperbolic tail of the detector pulse are realized (zero–pole cancellation networks[32,33]).

In Fig. 14 we show the circuit of the linear part of the electronics section of a multiwire proportional chamber (MWPC) designed to operate with small gas amplification at large loads. The first three BTs form a preamplifier. The capacitance C_1 in the emitter T_2 shortens the pulse characteristic of the preamplifier. The minimum duration of the output signal 10 nsec (at 0.1 of the amplitude) is attained for $C_1 = 130\,\text{pF}$.

The transistors T_4–T_6 form an amplifier–shaper with an input resistance of 50 Ω. The capacitance C_2 shortens the hyperbolic droop of the signal and is selected for specific detectors and gas mixtures.

The pulse characteristic of the entire section for $C_2 = 68$ pF has a duration of 12 nsec and a conversion coefficient of 2 μV/electron. For $C_D = 0$ we have the noise charge ENC $= 3 \times 10^3\ e^-$. It should be noted that this amplifier, which has the same time, amplitude, and noise characteristics as the circuit proposed in Ref. 34, is much simpler than the latter. The amplifier of Ref. 34 involves 20 transistors and 52 resistors.

High-speed gas detectors

The counting rate of a MWPC can be increased in the following ways:

1. By decreasing the anode–anode and anode–cathode separations. However, this involves significant technological problems.

2. By use of gas mixtures with large drift velocities.

3. By decreasing the gas-amplification coefficient (GAC). This requires the use of a low-noise amplifier.

The authors of Ref. 34 have studied various versions of MWPC constructions filled with "fast" gas mixtures based on freon-14 (CF_4) and hydrocarbons, and have achieved a loading rate of 2×10^6 particles/sec per wire. They stressed that it is necessary to use CF_4 of high purity. This gives rise to doubts, since this gas is electronegative. Nevertheless, it should be checked that domestically manufactured CF_4 can be used.

The measurements were carried out using three configurations of gas gaps for the mixture $CF_4 + 20\%$ C_4H_{10}. The amplifier shown in Fig. 14 (with inessential changes in the second cascade) was used in all three cases.

The counting and amplitude characteristics were measured according to the scheme of Fig. 15. The source S_1(^{106}Ru) mimicked the beam, and S_2(^{90}Sr) generated the background load; D are discriminators, CS is the coincidence scheme, and R is a rescaling device. The amplitude spectrum was measured by a 16-channel 12-bit ADC. The time resolution was measured from the delayed-coincidence curve. The GAC was determined from the amplitude of the signal from a ^{55}Fe source.

1. The MWPC (Ref. 35)

The anode–cathode gap is 4 mm, the anode–anode gap is 1 mm, the diameter of the anode wires is 10 μm, the diameter of the cathode wires is 100 μm, and the diameter of the sensitive region is 12 cm.

The counting characteristic has a plateau beginning at 4 kV with a width of more than 1.5 kV. At the beginning of the plateau the GAC is $\approx 10^3$. The pulse at the amplifier output has a symmetric bell shape of extent 20 nsec at the

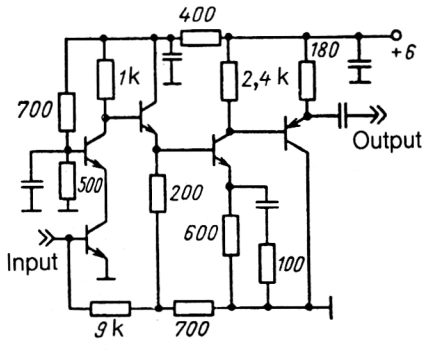

FIG. 12. Schematic diagram of a hybrid high-speed amplifier. All the *npn* transistors are of the type KT396, and the *pnp* ones are KT364. The capacitances are 10 nF.

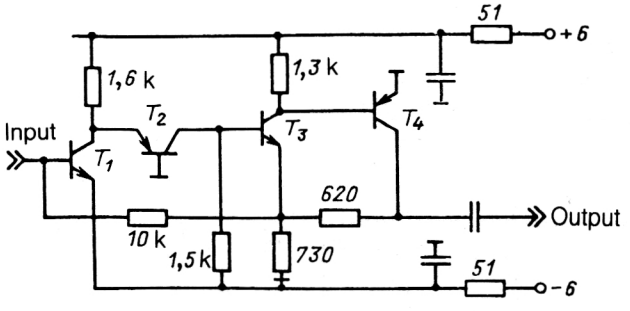

FIG. 13. Schematic diagram of a high-speed amplifier based on discrete elements. T_1 and T_3 are KT399 transistors, and K_2 and K_4 are KT363 transistors. All capacitances are 47 nF.

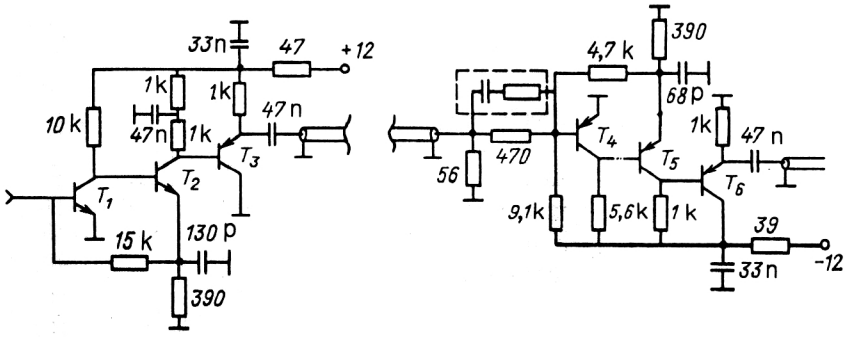

FIG. 14. Schematic diagram of an amplifier for high-speed gas detectors. T_1 is a KT399 transistor, T_2 is a KT371 transistor, and T_3–T_6 are KT363 transistors.

base. The amplitude spectrum has a shape close to the Landau distribution, and is practically undistorted for a background load of 0.5×10^6 particles/sec per wire, which when rescaled to minimally ionizing particles gives 1.6×10^6 particles/sec (Fig. 16). The time resolution (FWHM) is 6.7 nsec. The pickup at a neighboring wire is 20%–30% of the amplitude at the operating wire.

2. The minidrift chamber (Ref. 36)

The construction of the chamber is shown schematically in Fig. 17. The diameter of the sensitive region is 10 cm. The signal duration is 15 nsec with overshoot of opposite polarity equal to 20% of the amplitude. The amplitude spectrum is shifted toward small amplitudes by 10% for a background load of 1.3×10^6 particles/sec per wire (Fig. 18). The induction effect is 3%. The counting characteristic has a plateau from 1680 to 2030 V. The time resolution is 5 nsec.

3. A system of proportional tubes (Ref. 37)

The tubes were made of titanium of thickness 50 μm and had a diameter of 2 mm and a length of 10 cm. The anode had a diameter of 20 μm. The measurements were made with a system of 64 tubes. Modifications in the second cascade of the amplifier made it possible to decrease the response duration to 10 nsec. The tube characteristics are similar to those of the minidrift chamber.

The question of detector degradation owing to polymerization was not studied, but the small value of the GAC (10^3–10^4) suggests that the detectors have a long life. The data of Ref. 38 show that the mixture $CF_4 + 20\%$ C_4H_{10} is very stable to polymerization for large loads.

Therefore, the use of high-speed, low-noise amplifiers has made it possible to obtain a loading capability of 10^6 particles/sec per wire and a time resolution of 6 nsec, which makes it possible to use the MWPC for trigger-signal generation instead of hodoscopes of scintillation counters.

3. SIGNAL FILTERING

The signal-to-noise ratio is determined by the characteristics of the noise-reducing filter. In this section we consider various types of filters.

The maximum accuracy of amplitude measurements

The structure of the section which measures the signal from a detector can be represented as in Fig. 19. The signal-to-noise ratio η obtained at the section output is determined by the signal and noise spectra, the frequency characteristic of the filter F, and the type of converter P. The filter F for which the maximum possible η is obtained is referred to as the optimal filter. In the theory of optimal signal and noise filtering one usually considers the case where P is a peak detector, for which it can be shown that η cannot be larger than[39]

$$\eta \leqslant \left[\frac{1}{2\pi}\int_{-\infty}^{\infty}\frac{|U(\omega)|^2}{N(\omega)}\,d\omega\right]^{1/2}, \qquad (64)$$

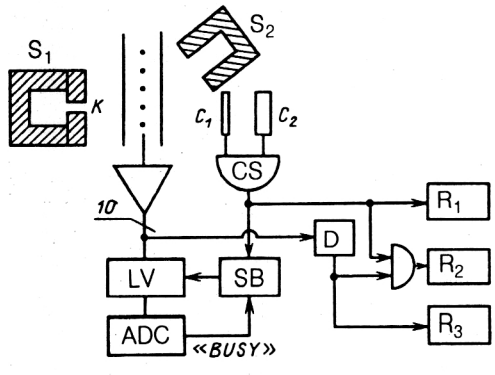

FIG. 15. Circuit for measuring the counting and amplitude characteristics of a chamber.

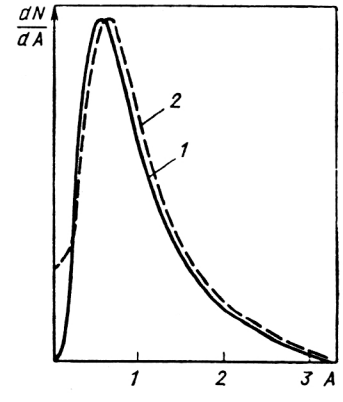

FIG. 16. Amplitude distributions of pulses from a chamber at low intensity (curve 1) and a load of 0.5×10^6 particles/sec per wire (curve 2).

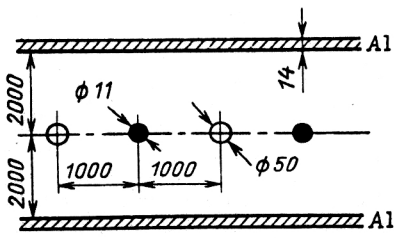

FIG. 17. Construction of the minidrift chamber. The dimensions are given in μm. The cathode is an aluminum foil of thickness 14 μm.

where $U(\omega)$ is the Fourier transform of the signal and $N(\omega)$ is the noise SD at the filter input. For example, if PA is a charge-sensitive preamplifier, then the equality in (64) is attained for a filter F having a "cusp" type of pulse characteristic:

$$H(t)=\exp(-|t|/\tau_c). \tag{65}$$

Physically realizable filters give an equivalent noise charge larger than that given by the optimal filter:

$$\mathrm{ENC}=\varkappa \mathrm{ENC}_{\mathrm{cusp}},$$

where $\mathrm{ENC}_{\mathrm{cusp}}$ is the equivalent noise charge obtained with the filter (65), and $\varkappa$ is the noise-excess coefficient. The inequality (64) implies that in the case of the peak detector all except the cusp filter have $\varkappa>1$. The peak detector is rarely used in practice. It is more common to work with a charge–digit converter, and sometimes more complicated converters are used.[40–44] This is because, as a rule, in experiments a trigger signal is present which can be used to trigger the converter. However, no one has managed to evade the limit (64). It is natural to ask whether or not values $\varkappa<1$ are possible for arbitrary P. In Ref. 45 we showed that the inequality (64) holds for an arbitrary law governing the converter P; only the form of the optimal filter will differ from (65).

In fact, the law governing the signal–digit converter can in general be written as

$$S=\int_{-\infty}^{\infty} P(t,t_m)V(t)dt, \tag{66}$$

where $P(t,t_m)$ is the converter algorithm; t_m is one or several parameters characterizing the time scale of this converter.

Performing the Fourier transforms

$$V(t)=\frac{1}{2\pi}\int_{-\infty}^{\infty} V(\omega)e^{j\omega t}d\omega; \tag{67}$$

$$P(t,t_m)=\frac{1}{2\pi}\int_{-\infty}^{\infty} P(\omega,t_m)e^{j\omega t}d\omega, \tag{68}$$

we rewrite (66) as

$$S=\frac{1}{2\pi}\int_{-\infty}^{\infty} V(\omega)P^*(\omega,t_m)d\omega. \tag{69}$$

Here we have taken into account the fact that $P(-\omega,t_m)=P^*(\omega,t_m)$, since $P(t,t_m)$ is a real function of

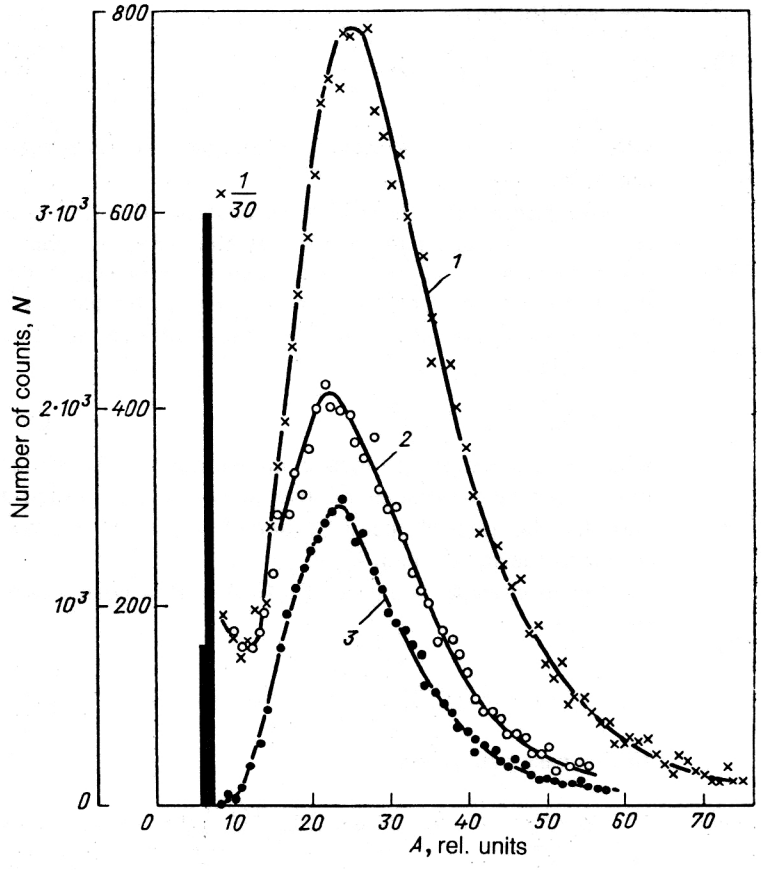

FIG. 18. Amplitude distributions of pulses from one wire at low intensity (curve 1) and a load of 1.3×10^6 particles/sec per wire (curve 2). Curve 3 is the amplitude distribution when the pulses from three wires at low intensity are summed. The pedestal, smeared by electronics noise, is shown by the dark line. The left-hand vertical scale refers to the spectrum (2). The voltage in the chamber is 1700 V.

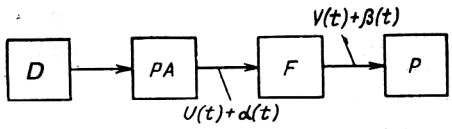

FIG. 19. Structure of the measuring section: *D*—detector; *PA*—preamplifier; *F*—filter; *P*—converter.

t. If $h(\omega)$ is the frequency characteristic of the filter, it is convenient to introduce the notation

$$F(\omega,t_m)=P^*(\omega,t_m)h(\omega) \tag{70}$$

and then (69) takes the form

$$S=\frac{1}{2\pi}\int_{-\infty}^{\infty} U(\omega)F(\omega,t_m)d\omega, \tag{71}$$

where $U(\omega)$ is the Fourier transform of the pulse shape at the input of F.

Similarly, for the noise we have

$$N=\int_{-\infty}^{\infty} P(t,t_m)\beta(t)dt. \tag{72}$$

Since $\langle\beta(t)\rangle = 0$, then $\langle N\rangle = 0$. Then the noise dispersion will be

$$D=\langle N^2\rangle = \int_{-\infty}^{\infty} dt \int_{-\infty}^{\infty} dt'\, P(t,t_m)P(t',t_m)K_\beta(t'-t), \tag{73}$$

where $K_\beta(t' - t) = \langle\beta(t)\beta(t')\rangle$ depends only on the difference $t' - t$, since the process $\beta(t)$ is stationary.

Going from the correlation function $K_\beta(t' - t)$ to the noise SD $N_\beta(\omega)$,

$$K_\beta(t-t')=\frac{1}{2\pi}\int_{-\infty}^{\infty} N_\beta(\omega)e^{j\omega(t-t')}d\omega, \tag{74}$$

and using the relation

$$N_\beta(\omega)=N_\alpha(\omega)|h(\omega)|^2, \tag{75}$$

where $N_\alpha(\omega)$ is the noise SD at the filter input, substituting (75) into (74) and (74) into (73), and using the definition (70), we obtain

$$D=\frac{1}{2\pi}\int_{-\infty}^{\infty} N_\alpha(\omega)|F(\omega,t_m)|^2 d\omega. \tag{76}$$

Using (71) and (76), we write the square of the signal-to-noise ratio as

$$\eta^2=\frac{1}{2\pi}\frac{\left[\int_{-\infty}^{\infty} U(\omega)F(\omega,t_m)d\omega\right]^2}{\int_{-\infty}^{\infty} N_\alpha(\omega)|F(\omega,t_m)|^2 d\omega}. \tag{77}$$

We introduce the notation

$$a(\omega)=|N_\alpha(\omega)|^{1/2}F(\omega,t_m);\qquad b(\omega)=|N_\alpha(\omega)|^{-1/2}U(\omega) \tag{78}$$

and rewrite (77) as

$$\eta^2=\frac{1}{2\pi}\frac{\left[\int_{-\infty}^{\infty} a(\omega)b(\omega)d\omega\right]^2}{\int_{-\infty}^{\infty}|a(\omega)|^2 d\omega}. \tag{79}$$

We use the Schwarz inequality

$$\left[\int_{-\infty}^{\infty} a(\omega)b(\omega)d\omega\right]^2 \leqslant \int_{-\infty}^{\infty}|a(\omega)|^2 d\omega \int_{-\infty}^{\infty}|b(\omega)|^2 d\omega. \tag{80}$$

The equality in (80) is attained for $a(\omega) = kb^*(\omega)$, where k is an arbitrary number, i.e., according to (78),

$$[h(\omega)P(\omega,t_m)]_{\text{opt}}=U^*(\omega)/N_\alpha(\omega). \tag{81}$$

Here

$$\eta\leqslant\eta_{\max}=\left[\frac{1}{2\pi}\int_{-\infty}^{\infty}\frac{|U(\omega)|^2}{N_\alpha(\omega)}d\omega\right]^{1/2}, \tag{82}$$

which exactly coincides with (64).

Therefore, for any type of converter P there exists an optimal filter F with transfer characteristic $h(\omega)$ given by (81). Here the maximum signal-to-noise ratio is the same as for the optimal filter–peak detector system.

The strobing integrator

The charge–digit converter (strobing integrator SI) is apparently most widely used in experiments. Its conversion law is of the form

$$S=\int_{t_0}^{t_0+\Delta} V(t)dt, \tag{83}$$

where t_0 is the time of opening of the gates and Δ is their duration.

In optimizing η it is necessary to position the gate relative to the signal in such a way that (83) is a maximum. For fixed Δ there is an optimal t_0. In fact, differentiating (83) with respect to t_0 and equating the derivative to zero, we obtain the condition (the stationary noise is independent of t_0)

$$V(t_0)=V(t_0+\Delta), \tag{84}$$

which has a simple geometric interpretation: the strobe pulse must be positioned relative to the signal in such a way that the times of opening t_0 and closing $t_0 + \Delta$ correspond to the same signal level.

Let us consider the case of a CSA with a noise SD of the form

$$N_\beta(\omega)=2kTg_m^2R_s\frac{1+\omega^2\tau_c^2}{\omega^2\tau_c^2}|h(\omega)|^2. \tag{85}$$

In this case (76) gives

$$D=\frac{1}{2\pi}\int_{-\infty}^{\infty} N_\beta(\omega)\frac{4\sin^2(\omega\Delta/2)}{\omega^2}d\omega. \tag{86}$$

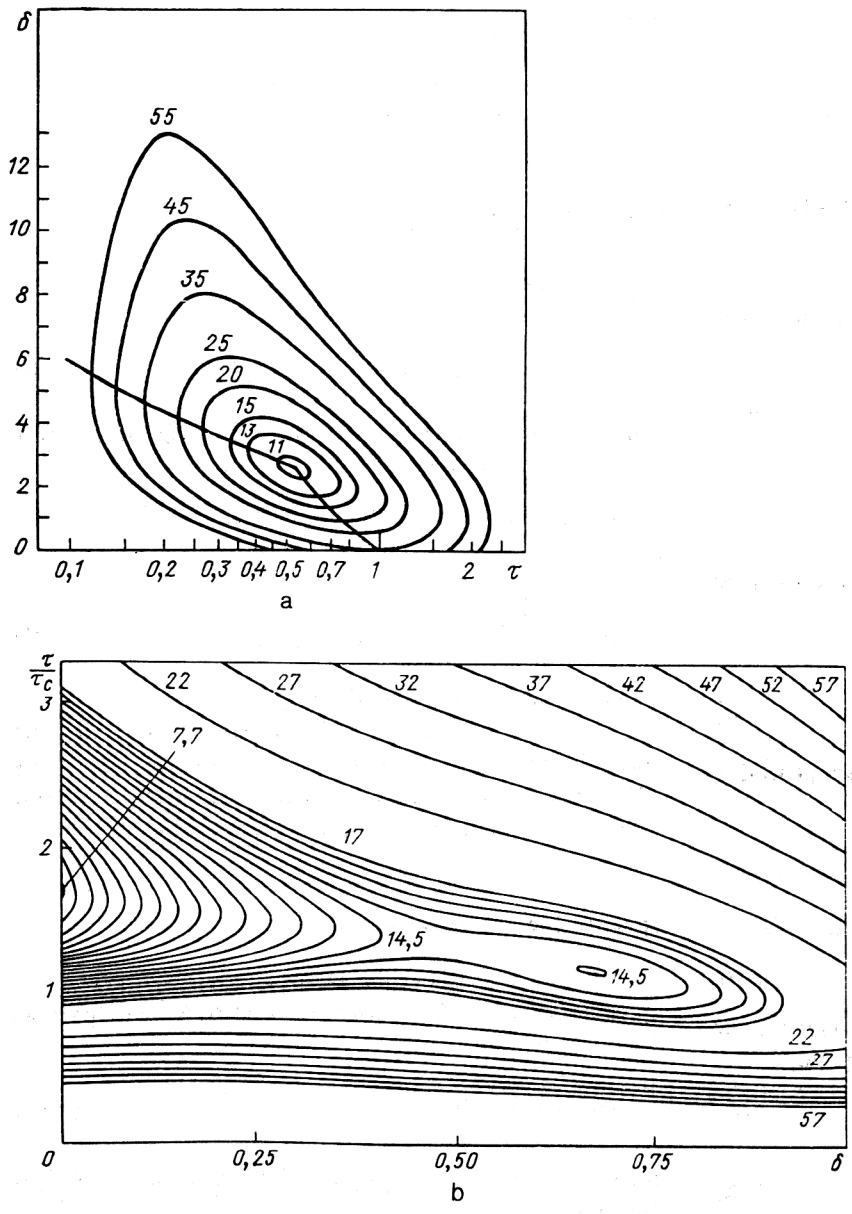

FIG. 20. Dependence of $\varkappa$ on τ/τ_c and $\delta = \Delta/\tau$ for the SI: (a) for *RC–CR* filtering; (b) for a triangular filter.

Equation (86) forms the basis for calculations of the ENC for SIs with *RC–CR* filtering[46] and for the triangle filter.[47] In Fig. 20a we show the dependence of $\varkappa$ on the shaping time τ/τ_c and the gate duration $\delta = \Delta/\tau$ for an *RC–CR* filter. The numbers near the curves are the values of $\varkappa - 1$ in %. We see that an optimum exists for $\tau = 0.5\tau_c$ and $\Delta = 2.5\tau$. Here $\varkappa_{\min} = 1.11$.

In working with a peak detector one of the best realizable filters is that with a triangular pulse characteristic. When the SI is used, this filter gives the $\varkappa$ shown in Fig. 20b. The minimum is attained for $\Delta = 0$ (the SI becomes a peak detector) and $\tau_{\text{opt}} = \tau_c\sqrt{3}$. Here $\varkappa_{\min} = 1.075$. It is interesting to note that $\varkappa$ has a second minimum on the right-hand side of Fig. 20b, but here $\varkappa \approx 1.14$.

One of the advantages of the SI over the peak detector is the decreased pile-up error.[46] Figure 21 illustrates how important it is to correctly choose the relative gate duration and the filter constant in order to decrease the signal duration. In all the cases shown in Fig. 21, $\varkappa$ is the same and equal to $e/2$ ($e = 2.718...$). The minimum duration is attained with $\tau = 0.17\tau_c$ for the *RC–CR* filter and $\tau = 0.44\tau_c$ for the triangular filter. Comparison of Figs. 21e and 21f with Fig. 21a shows that the use of the SI instead of the peak detector allows the loading capability of the detector to be increased by a factor of 4 to 5 without worsening the signal-to-noise ratio.

Other types of converters

These advantages of the SI suggest that other types of converters may also have advantages. The authors of Ref. 48 studied the structure of the measuring section shown in Fig. 22. Here F_1 is a filter, and F_2 is a block which converts the input signal into a digit according to some law. The

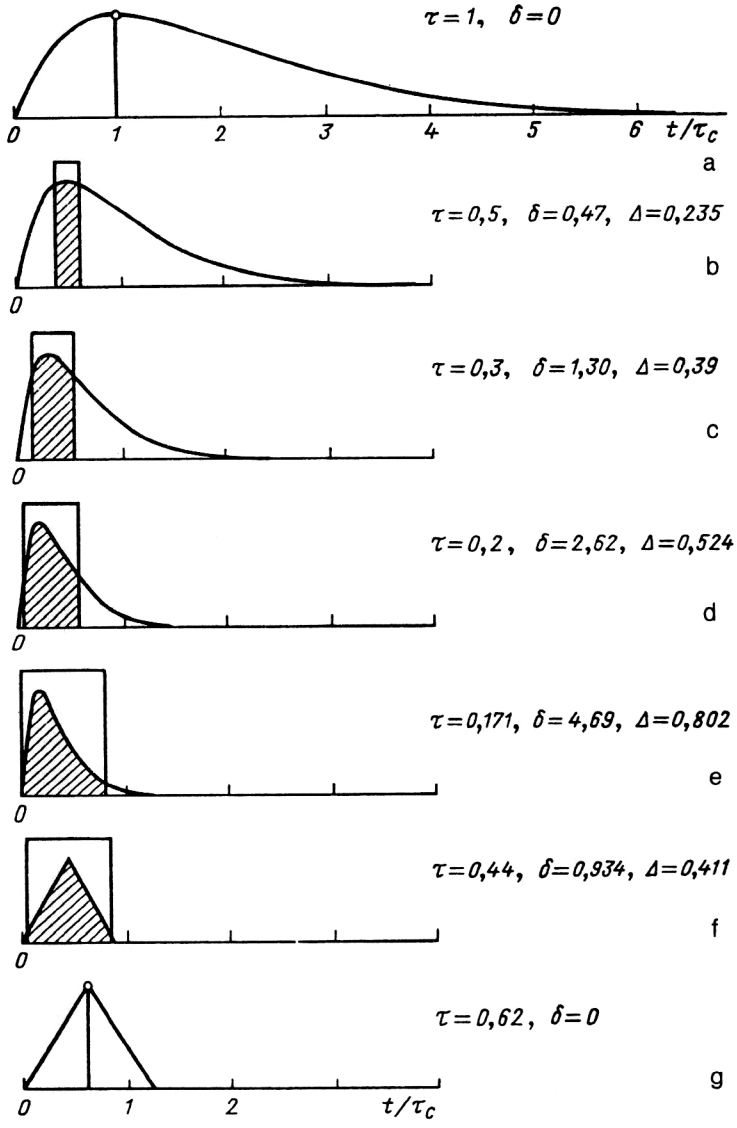

FIG. 21. Signal shapes at the SI input and relative positions of the strobe pulses (hatched regions) for which $\varkappa = e/2$ for an *RC–CR* filter (a–e) and the triangular filter (f, g).

system operates in the following manner. At the instant of time $t = 0$ the switch SW_1 is closed, and at the output of F_2 a signal $s(t)$ growing with time and noise with zero mean and increasing dispersion are observed. At the time t_s the switch SW_2 is closed for an infinitesimal time, i.e., the instantaneous value of the mixture of signal and noise is measured at its output. After this F_2 is returned to the initial state by the "Reset" command. We shall seek the optimal value of t_s and the optimal position of the signal relative to the time $t = 0$ for various types of F_1 and F_2.

1. F_1 is an ideal differentiator

If $h(t)$ is the pulse characteristic of the filter F_2, the noise dispersion is finite only for

$$h(0) = h(t_s) = 0, \quad h'(0) < \infty, \quad h'(t_s) < \infty. \tag{87}$$

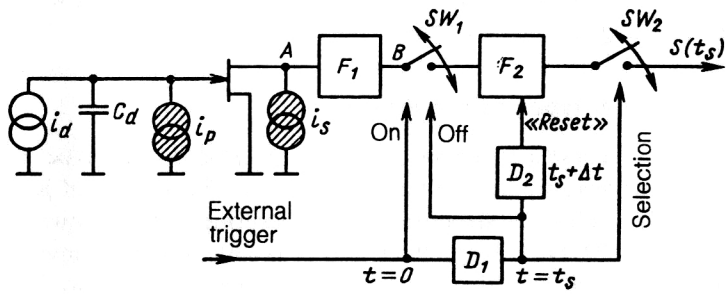

FIG. 22. Structure of the measuring section.

TABLE IV. Noise-excess factors $\varkappa$ for various filters with pulse characteristics $h(t)$.

$h(t)$	$\varkappa$	$\varkappa_{min}$
$(t_s-t)\exp(t/\tau_c)$, $0<t<t_s$	$\dfrac{\exp(t_s/\tau_c)}{[\exp(2t_s/\tau_c)-1]^{1/2}}$	1 for $t_s\to\infty$
$\sinh(2t_s/\tau_c)$, $t>0$	$\dfrac{[\sinh(2t_s/\tau_c)-2t_s/\tau_c]^{1/2}}{\sinh(2t_s/\tau_c)-(t_s/\tau_c)\exp(-t_s/\tau_c)}$	1 for $t_s\to\infty$
t, $0<t<t_s$	$\dfrac{(t_s/6\tau_c)^{1/2}}{1-\dfrac{\tau_c}{t_s}[1-\exp(-t_s/\tau_c)]}$	1,016 for $t_s=2{,}1\ \tau_c$

The ENC is written as a quadratic functional of $h(t)$. The solution of the variational problem gives the pulse characteristic of the optimal F_2 (Ref. 48):

$$h_{opt}(t)=\frac{\sinh(t/\tau_c)}{\sinh(t_s/2\tau_c)}, \tag{88}$$

where the signal should appear at the time γt_s, where $\gamma_{opt}=1/2$. Here

$$\varkappa^2=\frac{\sinh(2t_s/\tau_c)}{2\sinh^2(t_s/\tau_c)}\to 1 \quad \text{for } t_s\to\infty, \tag{89}$$

i.e., in this case the optimal filter cannot be realized, as in the case of the peak detector.

One of the realizable conversion laws is the triangle law:

$$h(t)=\begin{cases}2t/t_s, & 0<t<t_s/2;\\ 2-2t/t_s, & t_s/2<t<t_s.\end{cases} \tag{90}$$

Calculations show that for this law

$$\varkappa=[t_s/6\tau_c+2\tau_c/t_s]^{1/2}, \tag{91}$$

and the minimum is reached for $t_s=3.6\tau_c$ and is

$$\varkappa_{min}=1.075.$$

2. F_1 is a noise whitener

For the CSA it has the transfer characteristic of a differentiator with time constant τ_c. Now it is no longer necessary to satisfy the condition (87). The authors of Ref. 48 studied three types of converters for this filter. In Table IV we give the expressions for $h(t)$, $\varkappa$, and $\varkappa_{min}$.

The best present-day result was obtained for the last case (where the structure is whitener–switch–double integrator):

$$\varkappa_{min}=1.016.$$

Therefore, the charge–digit transformer makes it possible to increase the loading capability by several times in comparison with the peak detector without worsening the signal-to-noise ratio. Of the realizable filters, the best η is apparently obtained for the whitener–double integrator system, which can be realized using solid-state technology.

4. AMPLITUDE MEASUREMENTS FOR TRANSFORMER DETECTOR–AMPLIFIER COUPLING

Transformers are widely used in nuclear electronics to make the capacitance of the particle detector and the preamplifier coincide.[49–53] However, the transformer parameters (the standard size of the ferrite, the numbers of turns and their ratio, the shape and duration of the noise-elimination filter) are optimized empirically, since the existing methods of calculating transformer noise[51–55] are crude and ill-suited for practical use. The assumption that the transformer windings have infinite inductance, which was made in these references, automatically leads to the following: 1) divergence of the integral of the noise SD; 2) aperiodic response of the transformer, although an oscillatory mode is also possible. For these reasons the present theory, which is discussed in Refs. 51–55, cannot give any recommendations on how to optimize the transformer parameters. In this section we make a fairly rigorous study of a method of calculating transformer noise which eliminates the divergence of the SD integral noted in Refs. 53 and 54, and we develop practical recommendations for the choice of transformer parameters (the type of ferrite, the number of turns in the windings) and the shaping circuit (the type of filter and its time constant), depending on the experimental conditions. The material of this section is largely based on Refs. 56–59.

The transformer as a dissipative four-terminal network

A transformer is a dissipative element, since energy is lost in the core and the resistive windings. According to the fluctuation–dissipation theorem,[60–62] the transformer is also a source of noise. One method of calculating the noise SD of the core itself (the ferrite) is to use the methods of the theory of electric-field fluctuations.[61,62] We introduce external random electric and magnetic currents j_e and j_m. Then Maxwell's equations are written in the symmetric form

$$\operatorname{curl}\mathbf{E}=-\frac{1}{c}\frac{\partial\mathbf{B}}{\partial t}-\frac{4\pi}{c}\mathbf{j}_e; \tag{92}$$

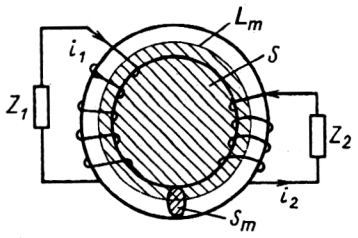

FIG. 23. Transformer coupling giving equal impedances of the detector Z_1 and the preamplifier Z_2. S_m and L_m are the effective cross section and length of the core, and S is the area of the loop L_m.

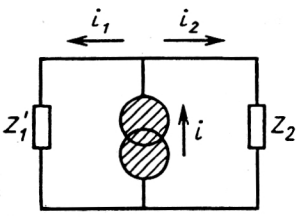

FIG. 24. Simplified equivalent circuit for calculating the thermal noise of the transformer for $\omega L_{1,2} \gg |Z_{1,2}|$.

$$\text{curl } \mathbf{H} = -\frac{1}{c}\frac{\partial \mathbf{D}}{\partial t} - \frac{4\pi}{c}\mathbf{j}_m. \tag{93}$$

Since in a conductor the displacement current is negligible compared with the conduction current, the term $\partial \mathbf{D}/\partial t$ can be discarded in (93). Inside the transformer we select two loops L_m (the effective length of the core) and L (the length of one turn) enclosing the areas S and S_m, respectively (Fig. 23). Then, assuming that the magnetic field is uniform over the cross section and zero outside it, we apply the Stokes theorem to (92) and (93), and, transforming to frequency space, we obtain

$$\varepsilon_i = \frac{j\omega\mu' HS_m}{c} - \frac{4\pi}{c} S_m j_m; \tag{94}$$

$$L_m H = (i_1 n_1 + i_2 n_2)4\pi/c, \tag{95}$$

where $\varepsilon_i = \oint E\, dL$ minus the emf induced in one turn, μ' is the real part of the magnetic permeability, i_1 and i_2 are currents, and n_1 and n_2 are the numbers of turns in the primary and secondary windings, respectively. Using the fact that

$$\varepsilon_i n_{1,2} = i_{1,2} Z_{1,2}, \tag{96}$$

from (94)–(96) we find

$$\varepsilon_i = -\frac{4\pi}{c^2}\frac{j\omega S_m \mu'}{L_m}\varepsilon_i\left(\frac{n_1^2}{Z_1} + \frac{n_2^2}{Z_2}\right) - \frac{4\pi}{c} j_m S_m. \tag{97}$$

Introducing L_0, the inductance per turn,

$$L_0 = -\frac{4\pi}{c^2}\frac{j\omega S_m \mu'}{L_m}, \quad L_{1,2} = L_0 n_{1,2}^2, \tag{98}$$

we transform (97) to the form

$$\varepsilon_i = \frac{4\pi}{c}\frac{j_m S_m}{1 + j\omega L_1/Z_1 + j\omega L_2/Z_2}. \tag{99}$$

To calculate the fluctuations of the noise voltages at the impedances $Z_{1,2}$ we use the well known expression of Ref. 62 for the spatial correlations of fluctuation magnetic fields:

$$\overline{j_m(r) j_m(r')} = kT\omega\mu'' \delta(r - r')/4\pi^2, \tag{100}$$

where μ'' is the imaginary part of the magnetic permeability, r and r' are the coordinates of the magnetic currents, and $\delta(r - r')$ is the Dirac delta function.

Averaging (100) over the ferrite volume $V_m = S_m L_m$, we obtain

$$\overline{j_{mv}^2} = kT\omega\mu''/(4\pi^2 S_m L_m). \tag{101}$$

The currents piercing the primary and secondary loops are

$$i_{1,2} = \varepsilon_i n_{1,2}/Z_{1,2}. \tag{102}$$

Then, taking into account (99) and (101), the SD of the noise current in the secondary loop can be written as

$$\overline{i_2^2(\omega)} = \frac{n_2^2}{|Z_2^2|}\overline{\varepsilon_i^2} = \frac{2kT\omega L_2 \tan\delta}{|Z_2^2||1 + j\omega L_1/Z_1 + j\omega L_2/Z_2|^2}, \tag{103}$$

where $\tan\delta = \mu''/\mu'$ is the tangent of the core loss. It is easy to see that the integral of the current SD converges. If we consider an ideal transformer with very large $L_{1,2}$ such that $\omega L_{1,2}/|Z_{1,2}| \gg 1$, then

$$\overline{i_2^2(\omega)} = 2kT\frac{1}{\omega L_2}\tan\delta\frac{|Z_1'|^2}{|Z_2 + Z_1'|^2}, \tag{104}$$

where $Z_1' = Z_1 n^2$ and the integral of (104) will have a logarithmic divergence.

From Eq. (104) we also find the equivalent circuit of Fig. 24, in which the noise SD is

$$\overline{i_2^2(\omega)} = 2kT\tan\delta/(\omega L_2). \tag{105}$$

This is the result which was used in Refs. 53–55.

In radio engineering core loops with an air gap are often used to improve the quality and discrimination. This actually makes it possible to decrease the tangent of the loss, $\tan\delta' = \tan\delta(\mu'/\mu)$, where μ' and μ are the original and effective permeability of the core and $\tan\delta$ is the loss without the gap. However, this does not improve the noise characteristics, as follows from Eq. (105).

Subcritical damping of the transformer

In this section we study a CSA which damps the transformer oscillations. As was shown in Refs. 57 and 58, a transformer with oscillatory and aperiodic modes gives a potentially identical ENC for optimal filtering. The circuit for analyzing the noise and the signal is given in Fig. 25a. Here i_d and C_1 are, respectively, the current and capacity of the detector [unless explicitly stated otherwise, $i_d = \delta(t)$]; $E_{1,2}$ are the noise voltage generators of the primary and

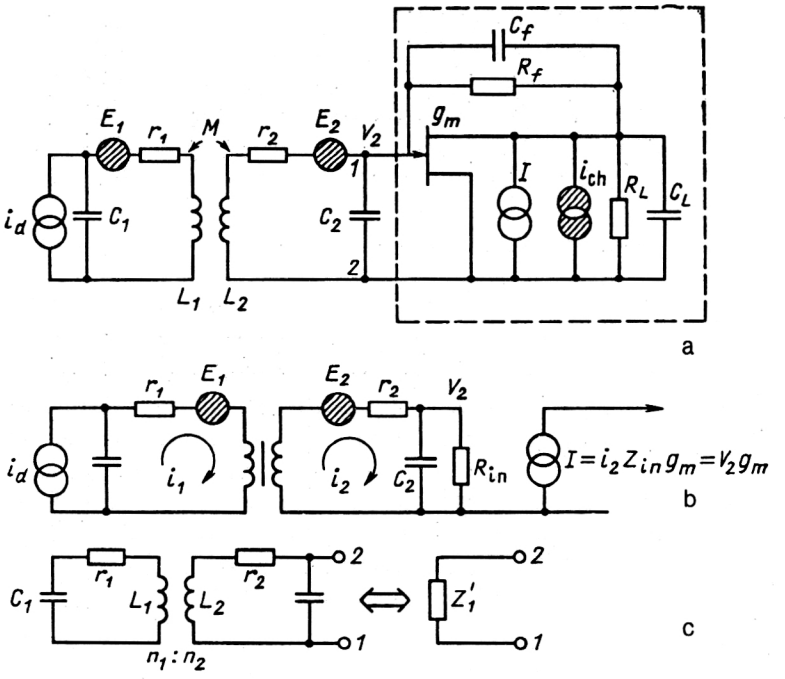

FIG. 25. Equivalent circuits for analyzing the thermal noise of the windings $E_{1,2}$ and the FET channel of the CSA for transformer coupling to a detector: (a) complete circuit; (b) simplified circuit including only $E_{1,2}$ and the signal i_d; (c) circuit for calculating the contribution of FET channel noise.

secondary windings. The noise SD of the primary and secondary windings and also the noise of the FET channel are, respectively,

$$\overline{E_{1,2}^2}=2kTr_{1,2};\quad \overline{i_{ch}^2}=2kTg_m, \tag{106}$$

where $r_{1,2}$ are the ohmic resistances of the primary and secondary windings and g_m is the FET transconductance. In the numerical calculations for the FET we used the following parameters of the FET 2N4861: $g_m = 20$ mA/V, $C_2 = 20$ pF. The frequency dependence of the thermal losses in the windings of the core with resistances $r_{1,2}$ was neglected (if the windings are made from multiple-strand Litz wire of diameter 40 μm, then $r_{1,2}$ will be frequency-independent up to 10 MHz), and E_1 and E_2 are assumed to be completely uncorrelated. The circuit of Fig. 25a does not contain a noise source describing the magnetic losses in the core, since its contribution will be estimated using the expression for the fluctuations of the loop current (103). The noise of the feedback resistor R_f can also be neglected, since the transformer connected to the CSA input shunts R_f by an equivalent resistance $r_{1,2}Q^2$, where Q is the transformer quality. In practical circuits[49,50] the condition $R_f \gg r_{1,2}Q^2$ is, as a rule, very easily satisfied. We assume that the magnetic permeability of the core is sufficiently high, $\mu \gg 1$, so that the coefficient of magnetic coupling between the windings can be set equal to unity.

The current I reflects the reaction of the FET to the voltage at its gate, $I = V_2 g_m$. In calculating V_2 from the sources i_d, $E_{1,2}$ we shall assume that the CSA (enclosed in the dashed box in Fig. 25a) can be replaced by a "cold" resistor $R_{in} = C_L/(C_f g_m)$. We therefore arrive at the equivalent circuit shown in Fig. 25b. The equations for the loop currents $i_{1,2}$ are

$$Z_1 i_1 + pMi_2 = E_1 + i_d/(pC_1); \tag{107}$$

$$Z_2 i_2 + pMi_1 = E_2, \tag{108}$$

where $M = K(L_1L_2)^{0.5}$, $K = 1$ is the coefficient describing the mutual inductance of the windings, and $Z_1 = pL_1 + r_1 + 1/(pC_1)$, $Z_2 = pL_2 + r_2 + L_{in}$ are the total series impedances of the primary and secondary loops. Taking into account the input capacitance of the FET C_2, the total input impedance of the CSA is [see Eq. (24)]

$$Z_{in} = [C_2(p + \beta_{in})]^{-1}, \quad \text{where } \beta_{in} = (R_{in}C_2)^{-1}.$$

Solving the system of equations (107)–(108), we write down the contributions to the loop current i_2 from the various sources:

$$i_2(i_d) = \frac{i_d M}{C_1 A(p)};\quad i_2(E_1) = \frac{E_1 pM}{A(p)};\quad i_2(E_2) = \frac{E_2 Z_1}{A(p)}, \tag{109}$$

where

$$A(p) = Z_1 Z_2 - p^2 M^2;$$

$$Z_1 = pL_1 + r_1 + 1/(pC_1);$$

$$Z_2 = pL_2 + r_2 + Z_{in}.$$

The components of the current of the FET of the CSA from the various signal and noise sources are found from Eqs. (9), (12), and (17):

$$\left.\begin{aligned} I(i_d) &= i_2(i_d) Z_{in} g_m; \\ I(E_1) &= i_2(E_1) Z_{in} g_m; \\ I(E_2) &= i_2(E_2) Z_{in} g_m. \end{aligned}\right\} \tag{110}$$

Let us consider the contribution of the noise of the FET channel. Let Z_1 be the impedance of the input circuit, which "sees" the CSA, i.e., the impedance across the terminals 1, 2 (Fig. 25c). It is easy to show that

$$Z_1 = (Z_1'Z_2' - Z_1'Z_c - p^2M^2)(Z_1'Z_2' - p^2M^2)^{-1} Z_c, \tag{111}$$

where

$$Z'_{1,2}=pL_{1,2}+r_{1,2}+1/(pC_{1,2}),\quad Z_c=1/(pC_2).$$

Then according to (18) at the CSA output the source of the current i_{ch} gives the following response:

$$I(i_{ch})=i_{ch}\frac{Z_1+Z_2+Z_3}{Z_1+Z_2+Z_3+Z_1Z_3g_m}, \tag{112}$$

where $Z_2=R_f\|C_f$, $Z_3=R_L\|C_L$, and Z_1 is given by (111). The contribution of the ferrite noise to the output current of the CSA can be found using Eq. (100) for the emf ε_i induced per turn. The value of ε_i is related to the impedances $Z''_{1,2}$ of the loads of the primary and secondary windings as

$$\varepsilon_i=\frac{4\pi}{c}\frac{U_f}{1+pL_1/Z''_1+pL_2/Z''_2}, \tag{113}$$

where

$$\overline{U_f^2}=2kT\omega L_2\tan\delta;\quad \tan\delta=\mu''/\mu',$$

$$Z''_1=r_1+1/(pC_1);\quad Z''_2=r_2+Z_{in}.$$

At the CSA output the noise emf ε_i gives the following value of the current:

$$I(f)=\varepsilon_i\frac{n_2g_mZ_{in}}{r_2+Z_{in}}. \tag{114}$$

The SD of the individual components of the noise are obtained after transforming from the Laplace variable p to $j\omega$ and multiplying Eqs. (110), (112), and (114) by their complex conjugates (denoted by the *):

$$\left.\begin{aligned}&H^2(E_1)=I(E_1)I(E_1)^*;\\&H^2(E_2)=I(E_2)I(E_2)^*;\\&H^2(i_{ch})=I(i_{ch})I(i_{ch})^*;\\&H^2(f)=I(f)I(f)^*.\end{aligned}\right\} \tag{115}$$

Since all the noise sources are independent, the SD of the total noise is equal to the sum of the SDs of the components:

$$N(\omega)=H^2(E_1)+H^2(E_2)+H^2(i_{ch})+H^2(f). \tag{116}$$

In Fig. 26a we give the SDs of the individual components of the noise at the current output of the CSA, calculated using Eqs. (115). The parameters used in the calculations are given in the caption of Fig. 26. The total SD of the noise from the transformer windings and the FET channel (the curve 1 + 2 + ch), the SD of the thermal noise of the ferrite (curve f), and the energy spectrum of the signal (S) are given in Fig. 26b. The minimum of the total noise SD is reached at the frequency $\Omega_T=6\times10^6$ sec^{-1}, the resonance frequency of the transformer loaded by the capacitances $C_{1,2}$. The depth of this minimum is determined by the sum of the noises of the FET channel and the transformer core. The frequency ω_0 is the eigenfrequency of the oscillations in the secondary loop. We see that for the K1 brand of ferrite (its characteristics are given in Table V) and the selected transformer and CSA parameters, the intrinsic ferrite noise can be neglected in the entire frequency range. The authors of Ref. 59 give the following criterion for choosing the type of ferrite for a given band of the head element of the CSA ω_T and desired duration of the shaped detector signal at the CSA output Ω_T^{-1}. The tangent of the core loss must satisfy the relation

$$\tan\delta\leqslant10\Omega_T/\omega_T. \tag{117}$$

Here the contribution to the total resolution due to the thermal noise of the core will be smaller than the total contribution of the noises from the windings and the FET channel. In Fig. 26b we also give the energy spectrum of the signal (S). We see that the noise minimum at the frequency Ω_T corresponds to the maximum of the signal spectrum, and it is therefore clear that simple filters of the RC–CR and $(RC)^2$–$(CR)^2$ type will be preferable over the others. The poles $p_{2,3}$ characterizing the signal transmission band can be estimated from the expressions

$$p_2=-0.5/(R_{in}C_2);\quad p_3=-R_{in}/L_2.$$

Optimization of the transformer for an amplifier with a cold resistor

The transformer is optimized through two parameters: the energy resolution (ENC) and the loading capability, i.e., the signal duration.

The ENC calculations were carried out using Eq. (61), where $N(\omega)$ is given by (116), $S(\omega)$ is the Fourier transform of the detector signal at the CSA output [the first of Eqs. (110)], and $F(\omega)$ is the transfer characteristic of the filter [RC–CR or $(RC)^2$–$(CR)^2$].

Choice of the filter parameters

In Fig. 27 we give the calculated dependence of the ENC on the detector capacitance C_1 for three values of the inductance L_2 and two values of the "cold" resistance of the CSA, R_{in}. Curves 1–4 correspond to the $(RC)^2$–$(CR)^2$ filter, and curve 5 to the RC–CR filter. We see that the use of the two-cascade integrator–differentiator makes it possible to improve the ENC by roughly a factor of two over the case when the one-cascade variant is used. In Table VI we give the dependence of the total noise charge and its individual components for an $(RC)^2$–$(CR)^2$ filter.

The location of the maximum of the transfer characteristic of the filter τ is varied relative to the minimum of the noise SD. From Table VI we see that: the minimum of the ENC is reached at $\tau^{-1}=\Omega_T$, as expected from the symmetry of the noise SD (Fig. 26b), and therefore below we shall always take $\tau^{-1}=\Omega_T$, unless stated otherwise; the largest contribution to the ENC comes from FET channel noise when an hf ferrite is used; the ENC is not critically sensitive to small deviations of τ^{-1} from Ω_T, which considerably simplifies the tuning of practical circuits.

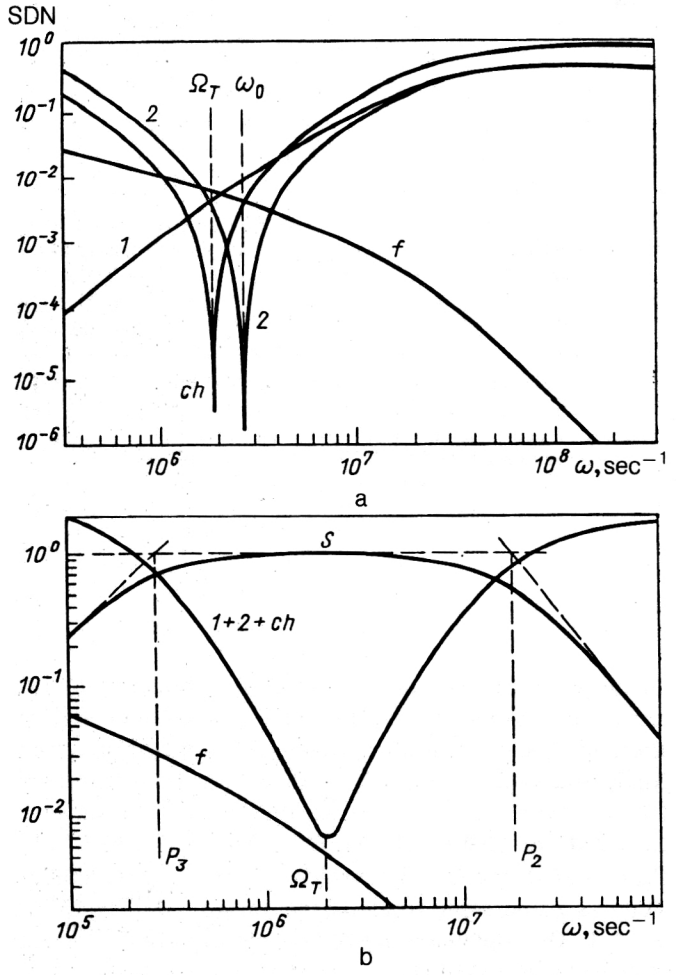

FIG. 26. Results of calculations of the noise and frequency characteristics of an amplifier with transformer coupling to a detector: (a) noise SDs of the primary and secondary windings (curves 1 and 2, respectively), the FET channel (ch), and the ferrite (f); (b) energy spectrum of the signal (S) and SD of the sum of the noise from the FET channel and the two windings (1 + 2 + ch), and SD of the K1 ferrite (f). CSA and transformer parameters: C_2 = 20 pF, q_m = 20 mA/V, C_1 = 2 nF, L_2 = 0.7 mH, $n_2/n_1 = 141/20$.

Comparison of transformer and galvanic detector–amplifier couplings

Comparison of the different variants only in terms of the ENC is clearly inadequate, since at high counting rates the error is largely determined by the pile-up noise, which, in turn, depends on the shape and duration of the output signals of the filter. In order to decrease the number of parameters, it is desirable to introduce a definition of the signal duration which ignores the signal shape. As such a definition we chose the duration at a level of $+0.1$ or -0.1 of the maximum value (the larger of the two). Of course, this definition is somewhat arbitrary, but it is convenient for measurements.

Let us compare filters of the RC–CR or $(RC)^2$–$(CR)^2$ type for transformer coupling and of the RC type for galvanic coupling. In both cases the current output of the CSA is used. Oscillograms of signals of the same duration at the outputs of these filters are shown in Fig. 28, where the horizontal axis is measured in dimensionless units of Ωt, αt, and $\Omega = 1.6\alpha$, $\alpha^{-1} = R_{\text{in}}C_1$. The filter duration in all cases corresponds to the minimum of the noise SD, Ω_T^{-1}. In Fig. 29 we compare the ENC for galvanic coupling (curve 1) and transformer coupling using a K1 hf ferrite (curve 2) at the same signal duration. The inductance L_2 was varied, and the numbers along curve 2 indicate the number of turns for which the condition of equal signal durations $\Omega_T^{-1} = 0.6R_{\text{in}}C_1$ is satisfied.

TABLE V. Characteristics of ferrites. Definitions: f', f'' are the frequencies at which $\tan\delta = \mu''/\mu'$ is equal to 0.1 and 0.02, respectively; μ'' and μ' are the real and imaginary parts of the magnetic permeability; μ_i is the original magnetic permeability.

Brand of ferrite	Manufacturer	f', MHz	f'', MHz	μ_i
K1	Siemens	25	18	80
3B7 (N28)	Philips (Siemens)	0.6	0.2	2300
3D3 (M33)	Philips (Siemens)	1.5	0.8	650
50 VCh2	USSR	60	35	50

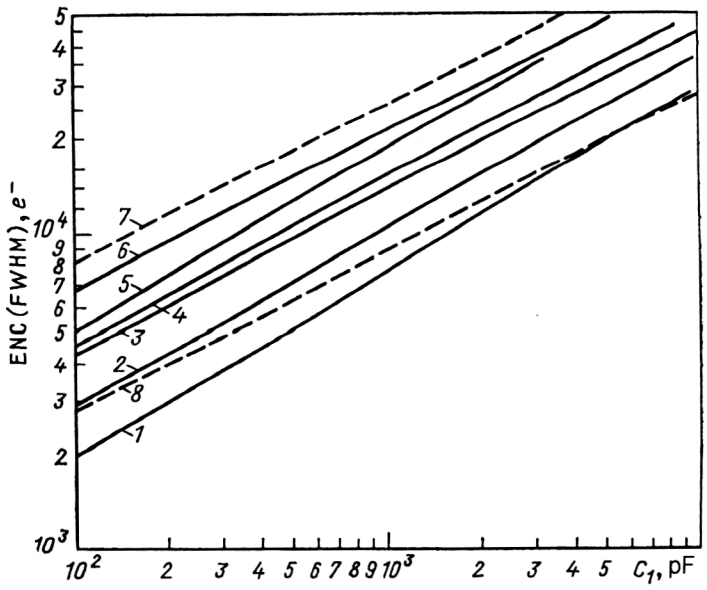

FIG. 27. Dependence of the ENC on the detector capacitance and on the parameters of the transformer and the filter for transformer (1–6) and galvanic (7, 8) couplings: (1) $L_2 = 35$ mH, $R_{in} = 200$–$2000\ \Omega$; (2) $L_2 = 3.5$ mH, $R_{in} = 200$–$2000\ \Omega$; (3) $L_2 = 0.35$ mH, $R_{in} = 1400\ \Omega$; (4) $L_2 = 0.35$ mH, $R_{in} = 200\ \Omega$; a filter of the $(RC)^2$–$(CR)^2$ type was used for curves 1–4; (5) $L_2 = 35$ mH, $R_{in} = 200\ \Omega$, filter of the RC–CR type; curves 1–6 pertain to a K1 ferrite; (6) $L_2 = 3.5$ mH, $R_{in} = 2000\ \Omega$, filter of the $(RC)^2$–$(CR)^2$ type; (7) $R_{in} = 200\ \Omega$; (8) $R_{in} = 2000\ \Omega$. Curves 7 and 8 pertain to galvanic coupling of the CSA and the detector with a sequential RC filter whose time constant is $R_{in}C_1$.

The role of "cold" CSA resistance

It follows from Fig. 27 that in the case of transformer coupling R_{in} has practically no effect on either the ENC or the signal duration. However, as R_{in} is decreased it is possible to decrease L_2, and, accordingly, the external dimensions of the transformer, while satisfying the damping condition $L_2 \geqslant 8R_{in}^2C_2$ (C_2 is the input capacitance of the CSA). Here the duration decreases as $L_2^{-1/2}$, but since ENC $\sim L_2^{-1/6}$, the gain in the duration can turn out to be more important than the small gain in the ENC. For example, for a K1 ferrite and $C_1 = 10$ nF (the results of the calculations are given in Table VII), the ENC was increased by a factor of 2, and the signal duration was decreased by a factor of 25 as R_{in} was decreased from 1000 to 40 Ω. Therefore, it is useful to use a CSA with small R_{in} at large capacitances and high counting rates.

The limit on the inductance owing to finite duration of the detector signal

Up to now it has been assumed that the detector signal is a δ function. For a finite signal duration it is necessary to increase the inductance L_2, since frequencies smaller than R_{in}/L_2 are not passed by the transformer (Fig. 26b). Let us assume that the detector signal is an exponential with time constant ε^{-1}. The inductance L_2 should be such that the condition $\varepsilon \geqslant \Omega_T$ is satisfied, since for $\varepsilon \leqslant \Omega_T$ the ENC grows linearly with increasing detector-signal duration (Fig. 30). This fact complicates the design of a transformer for making a detector with a slow response (for example, one based on pure argon) compatible with a CSA.

The contribution of the winding resistance

An increase of the winding inductance, which is desirable for a number of applications, can be obtained by increasing the external dimensions of the core or the number of turns. The first method is not always possible, and, moreover, the core parameters are chosen so that the inductance per turn A_L increases weakly with increasing external dimensions. We are therefore left with the second alternative, and this leads to making the turns from a thin conductor. Calculations show that for the N28 ferrite ($A_L = 1600$ nH, $n_2/n_1 = 350/32$) for a detector capacitance $C_1 = 2$ nF and CSA parameters $C_2 = 20$ pF, $g_m = 20$ mA/V, $R_{in} = 200\ \Omega$, the ENC grows from 7 to 10 thousand electrons as ρ increases from 0.0145 to 0.58 Ω. The value $\rho = 0.58\ \Omega$ is the resistance of a single strand of Litz wire of diameter 40 μm, and $\rho = 0.0145\ \Omega$ is the resistance of 40 such strands connected in parallel.

Choice of the number of turns

In the case of an ideal transformer ($L_{1,2} = \infty$, $r_{1,2} = 0$) it is easy to show that the ENC minimum is reached for the turn ratio $K = n_2/n_1$ satisfying the following condition on the detector and preamplifier capacities:

$$K_{opt} = (C_1/C_2)^{0.5}. \qquad (118)$$

Here the intrinsic frequencies in the loops of the two windings are equal. As was shown in Ref. 63, when there is parallel noise in the head element of the CSA the optimal value for K can differ significantly from (118). However, all the conclusions of Ref. 63 are based on the assumption of an idealized core ($L_{1,2} = \infty$, $r_{1,2} = 0$, no ferrite noise). The dependence ENC(n_1,n_2) has been studied numerically for a real transformer. In Fig. 31 we show the results of calculations of ENC(n_1,n_2) for a K1 ferrite at the capacities $C_1 = 200$ and $C_2 = 20$ pF. It was assumed that the signal extracted from the current output of the CSA passes through an $(RC)^2$–$(CR)^2$ filter with time constant Ω_T^{-1}. The main conclusions which can be drawn on the basis of Fig. 31 and analysis of the results of the calculations made in Ref. 59 for cores of N28 and K1 ferrites at the capacities $C_1 = 200$ pF and 2 nF are the following:

1. The ENC is not very sensitive to a deviation of K from K_{opt}; a decrease of n_2 by a factor of two from the optimal value increases the ENC by 20%.

2. For a low-frequency ferrite it is advantageous to decrease K from K_{opt} at the expense of increasing n_1.

Comparison of the calculations and experiment

The presence of a characteristic dip in the noise spectral characteristic makes it very easy to compare the calculations with experiment. In Fig. 32 we show the results of measurements and calculations of the noise SD for a ferrite of the brand 50VCh2.

The measurements were made by a V6-1 selective voltmeter, which measures not the SD, but the effective value of the noise in a narrow frequency band (10 kHz). Therefore, along the horizontal axis in Fig. 32 we show the square roots of the calculated noise SD. The points show the measured values. Absolute meaurements of the SD were not carried out; the measured values were shifted along the horizontal axis relative to the calculated values so as to obtain the best (visual) agreement. We see that the positions and depths of the experimental minima coincide with the calculated values, although the shapes of the curves are different.

In Fig. 33a we give the calculated and experimental values of the ENC for the 3V7 ferrite and a standard CSA (Ref. 50) with subsequent $(RC)^2$–$(CR)^2$ shaping ($\tau_{CR} = 1.7$ μsec, $\tau_{RC} = 240$ nsec). The calibration pulse mimicked the signal of a liquid-argon detector—an exponential with time constant equal to 250 nsec. The experimental data were obtained by G. Spandre and F. Sergiampietri (INFN, Pisa, Italy) and are reproduced here with their kind permission. The authors have obtained similar noise characteristics for the K1 hf ferrite (with winding inductances $L_2 = 900$ μH, $L_1 = 32$ μH) with detector–preamplifier coupling. The detector capacitance was fixed at $C_1 = 1.8$ nF, and the CSA was similar to that described in Ref. 50. The signal extracted from the current output of the CSA was fed to a filter with adjustable time constant. In Fig. 33b we show the dependence of the ENC on the shaping time for fixed parameters of the detector, the transformer, and the preamplifier, and compare it with the calculated dependence. We see that the minimum of the ENC is reached for a shaping duration corresponding to the inverse of the frequency of the minimum of the noise SD.

CONCLUSIONS

Above, we attempted to answer a number of practical questions arising in the design of the transformer coupling of a detector and a preamplifier. The main result can be stated briefly: there is practically no freedom of choice, and the calculation gives the following simple rules:

1. If we assume that the detector capacitance C_1 and the durations of the detector (ε^{-1}) and filter (T_f) pulses are specified by the experimental conditions, then the inductances of the transformer windings when the damping conditions are satisfied are determined by the more stringent of the two relations

$$\varepsilon^{-1} \leqslant \Omega_T^{-1} = (L_1 C_1)^{0.5}, \quad T_f \cong 7\Omega_T^{-1}.$$

The free parameters are the input resistance of the CSA depending on the circuit configuration, $R_{in} \cong 0.2$–2 kΩ, the transconductance of the transistor, $g_m = 5$–50 mA/V, and the transistor input capacitance $C_2 = 5$–50 pF. The last two parameters are related.

2. The duration of the signal output by the filter also determines the possible set of ferrite types, namely, a ferrite is needed which satisfies the condition (117):

$$\tan\delta \leqslant 10\Omega_T/\omega_T.$$

3. The total noise of the FET channel and the windings is ENC $\sim L_2^{-1/6}$, i.e., it depends weakly on the type of ferrite.

4. For $C_1 \leqslant 300$ pF the use of a transformer is inappropriate.

5. If the experimental conditions permit low counting rates, the use of a transformer can prove to be harmful—a transformer does not permit the ENC to be decreased.

6. Conversely, at high counting rates it is useful to employ transformer coupling to reduce pile-up noise.

5. CROSS-TALK IN IONIZATION CALORIMETERS

An ionization calorimeter is a system of electrodes segmented both longitudinally and transversely (along the direction of motion of the particles), i.e., it is actually made up of a large number of individual ionization chambers, each of which is loaded by its own amplifier. In the ideal case the chambers do not know about each other, but in

TABLE VI. Dependence of the ENC (FWHM) of 10^3 e^- and its individual components on the location of the maximum of the transfer characteristic of an $(RC)^2$–$(CR)^2$ filter relative to the minimum Ω_T of the noise SD. ENC(1), ENC(2), ENC(ch), and ENC(f) are, respectively, the components of the ENC associated with the primary and secondary windings, the FET channel, and the ferrite. The inductance of the secondary winding is $L_2 = 4.4$ mH, the transformer ratio is $n_2/n_1 = (C_1/C_2)^{0.5} = 7$, K1 ferrite, $R_{in} = 1$ kΩ, $C_1 = 1$ nF, $C_2 = 20$ pF, $g_m = 20$ mA/V, $r_2 = 25$ Ω; δ-function signal. The filter poles are multiples of $\tau_{RC} = \tau_{CR} = \tau$.

τ^{-1}	ENC (1)	ENC (2)	ENC (ch)	ENC (f)	ENC
Ω_T	3.1	3.2	7.5	3.2	9.3
0.5 Ω_T	2.4	8.0	10.8	6.1	15.0
2 Ω_T	4.2	3.7	10.8	1.7	12.3

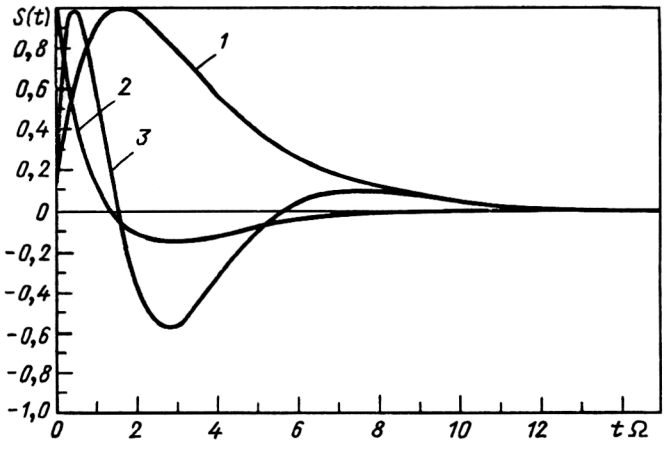

FIG. 28. Shapes of signals at filter outputs: 1—galvanic coupling; 2 and 3 are, respectively, for RC–CR and $(RC)^2$–$(CR)^2$ filters. The dimensionless quantity Ωt is plotted along the horizontal axis.

reality if a particle passes through the ith chamber, a signal can appear in the kth electronics channel. This phenomenon is usually referred to as cross-talk. It should be noted that cross-talk, in contrast to electronics noise and electromagnetic cascade fluctuations, grows in proportion to the energy release in the calorimeter. Therefore, the total energy and coordinate resolution of full-absorption spectrometers operating in beams of high-energy particles will be very sensitive to the level of cross-talk in electronics channels.

The following basic principles governing the development of cross-talk can be stated.

1. Falloff of the voltage at common impedances of the channels

In principle, this can be avoided if a separate anode–amplifier–cathode loop is made for each ionization chamber. However, this is an expensive alternative, since it requires the use of a high-voltage bypass capacitor and two pressure-seal feed-throughs on each chamber. If the bypass capacitor is located on the outside of the cryostat, then one of the pressure-seal feed-throughs must be high-voltage, which is unacceptable in most cases. If the capacitor is placed inside, the following difficulties arise: first, the capacitor must withstand cooling (when the detector is filled with a condensed noble gas); second, its capacitance here must remain high compared with that of a gap; and, third, in liquids with electron conductance there are always free electrons and/or ions which under the action of the field are transported along the surface of the capacitor, thereby inducing excess noise. This effect depends strongly on the type of dielectric and is practically unstudied. Moreover, the charge redistribution on the capacitor surface leads to breakdown, and, for example, in liquid argon the breakdown voltage becomes several times lower than in liquid nitrogen. The authors of Ref. 50 described a liquid-argon calorimeter in which the bypass capacitor common to 16 chambers is located on the outside of the cryostat, and a high voltage is introduced via a single common pressure-seal feed-through. Here a voltage appears on the common impedance, owing to the intrinsic capacitive resistance of the capacitor, the finite ohmic resistance of the conductors, and the induction of the generated loop arising because of the finite dimensions of the capacitor. The coincidence scheme is shown in Fig. 34a. If it is assumed that a CSA with "cold" resistance has an active input resistance R and an input capacitance C', then the measuring section can be represented as the equivalent circuit of Fig. 35a. We introduce the following notation: N is the number of channels with common impedance Z_0, C is the capacitance of one chamber, and I_k is the signal in the kth chamber:

$$R_p=R/(N-1);\quad C_p=C(N-1);\qquad C'_p=C'(N-1). \tag{119}$$

Upon the appearance of a signal I, loop currents I_n arise in the other channels:

$$\left.\begin{aligned} I_k&=I(pC)^{-1}(R+Z_0\|Z_p)^{-1};\\ I_n&=I(pC)^{-1}(R+Z_0\|Z_p)^{-1}Z_0(Z_0+Z_p)^{-1},\end{aligned}\right\} \tag{120}$$

where $Z_p = R_p + (pC_p)^{-1}$ and the capacitance C' is neglected. The transfer functions of the pickup in neighboring channels in the current and the voltage are

$$K_I(p)=\frac{I_n}{I_k}=\frac{Z_0}{Z_0+Z_p}; \tag{121}$$

$$K_U(p)=\frac{U_n}{U_k}=\frac{K_I(p)}{N-1}=\frac{1}{N-1}\frac{Z_0}{Z_0+Z_p}. \tag{122}$$

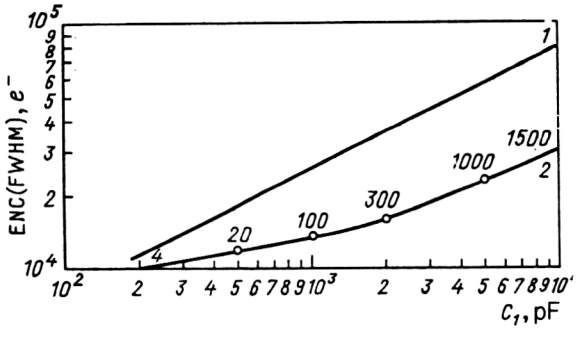

FIG. 29. The dependence ENC(C_1) for galvanic (curve 1) and transformer (curve 2) coupling. The numbers near curve 2 are the numbers of turns n_2 in the secondary winding. The resistance per turn is $\rho = 0.058\ \Omega$. For all cases $R_{in} = 200\ \Omega$. The filters are of the type $(RC)^2$–$(CR)^2$ and RC, respectively, for the transformer and galvanic coupling.

TABLE VII. ENC (FWHM), $10^3\,e^-$ for two values of R_{in} and two types of ferrite as a function of the detector capacitance C_1. The resistances of the windings were chosen to be $r_2 = \rho n_2$, $r_1 = r_2(n_1/n_2)^2$, $\rho = 0.058\ \Omega$. The inductance is L_2 = var, and it was required that the condition $\Omega_T^{-1} = 0.6R_{in}C_1$ hold for both ferrites.

C_1, pF	K1		N28	
	$R_{in} = 40\ \Omega$	$R_{in} = 1000\ \Omega$	$R_{in} = 40\ \Omega$	$R_{in} = 1000\ \Omega$
200	34,5	6,1	145	24,5
500	31,6	6,8	124	16,2
1000	31,9	7,8	117	12,4
2000	33	9,2	113	11
5000	34,7	12,4	102	11
10 000	36,7	16,4	85	12

Alternatively, in the case of the impedance $Z_0 = pL_0$, we have

$$K_i(p) = \frac{pL}{pL_0 + R_p + (pC)^{-1}} = \frac{p^2}{(p-p_1)(p-p_2)}. \tag{123}$$

If the poles $p_{1,2}$ are located far beyond the poles of the noise-reduction filter, then (123) can be simplified considerably:

$$K_I(p) = p^2/(p_1p_2) = L_0C_pp^2. \tag{124}$$

Here the pickup in neighboring channels will have the form of the second derivative of the signal with respect to the time:

$$U_n(t) = L_0C_p\ddot{U}_k(t)/(N-1) = L_0C\ddot{U}_k(t). \tag{125}$$

The case of the common impedance $Z_0 = pL_0 + (pC_0)^{-1}$ is most widespread in practice. For it,

$$K_I(p) = \frac{pL_0 + (pC_0)^{-1}}{pL_0 + R_p + (pC_t)^{-1}} = \frac{p^2 + (L_0C_0)^{-1}}{p^2 + pR_p/L_0 + (L_0C_t)^{-1}}, \tag{126}$$

where $C_t = C_0C_p(C_0 + C_p)^{-1}$ is the equivalent capacitance of the loop. The poles are

$$p_{1,2} = -\frac{R_p}{2L_0}\left\{1 \mp \sqrt{1 - \frac{4L_0}{R_p^2C_t}}\right\}. \tag{127}$$

If $p_{1,2}$ are located far beyond the poles of the noise-reduction filter, then (126) simplifies:

$$K_I(p) = [p^2 + (L_0C_0)^{-1}]/(p_1p_2) = L_0C_tp^2 + C_t/C_0. \tag{128}$$

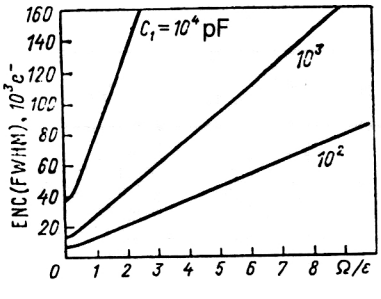

FIG. 30. Dependence of the ENC on the ratio Ω_T/ε, where Ω_T is the frequency at which the noise SD has a minimum and ε^{-1} is the time constant of the detector signal for various C_1.

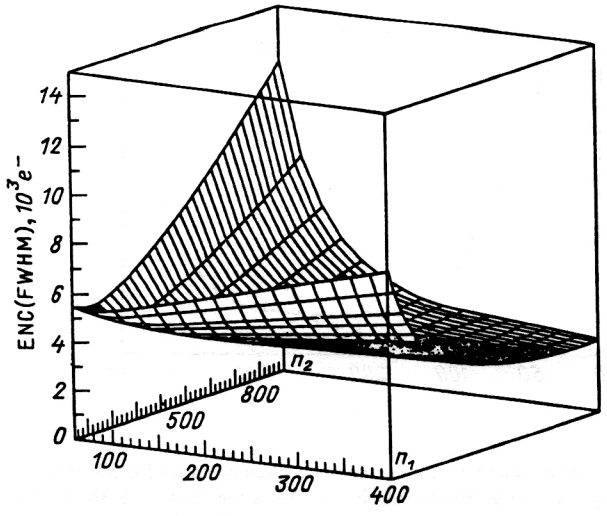

FIG. 31. The dependence ENC(n_1,n_2) for transformer coupling with a K1 ferrite.

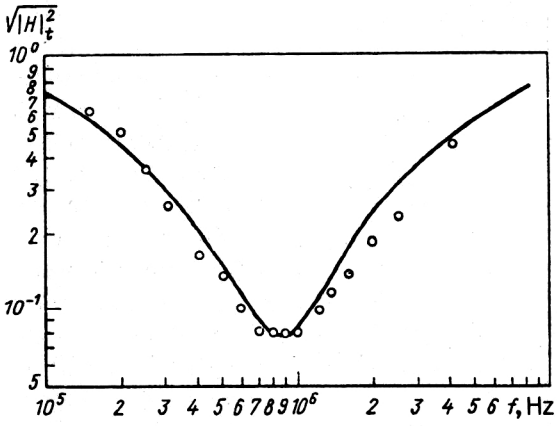

FIG. 32. Square roots of the noise SD at the CSA output. The curves are calculated, and the points are measured values. Transformer and circuit parameters: $n_1/n_2 = 23/230$, inductance per wire $A_L = 35$ nH, $C_1 = 100$ pF, $R_{in} = 300\,\Omega$.

The pickup at neighboring channels is the sum of two functions, one of which has the shape of the signal, and the other is proportional to its second derivative:

$$U_n(t) = L_0 C_t \ddot{U}_k(t) + C_t/C_0 U_k(t). \tag{129}$$

Repeating the same calculations for the case $Z_0 = pL_0 + R_0$, we obtain

$$U_n(t) = R_0 C[L_0/R_0 \ddot{U}_k(t) + \dot{U}_k(t)]. \tag{130}$$

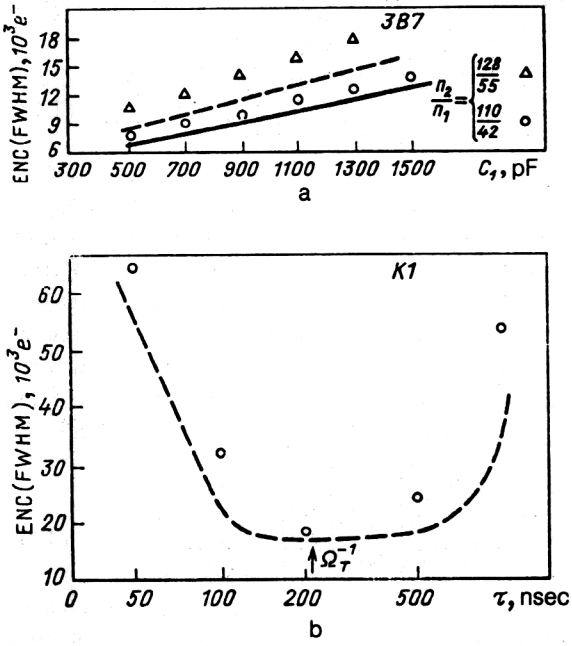

FIG. 33. Experimental data on the noise characteristics for transformer coupling: (a) the dependence ENC(C_1) for a low-frequency 3B7 ferrite for two winding ratios: 128/55 (△) and 110/42 (○). The solid and dashed lines are the calculation; (b) comparison of the calculated dependence ENC(τ) (dashed line) with experiment (○), where τ is the time constant of the $(RC)^2$–$(CR)^2$ filter, and $C_1 = 1.8$ nF.

Let us give the expressions for the transfer characteristics of the pickups due to the voltage drop at the inductance L_0,

$$K_{U1}(p) = \frac{p^2}{(p-p_1)(p-p_2)}, \tag{131}$$

the capacitance C_0,

$$K_{U2}(p) = \frac{C_t}{C_0}\frac{p_1 p_2}{(p-p_1)(p-p_2)}, \tag{132}$$

and the active resistance R_0,

$$K_{U3}(p) = \frac{R_0}{R_p}\frac{p_2 p}{(p-p_1)(p-p_2)}. \tag{133}$$

The Bode diagrams of the transfer characteristics (131)–(133) are given in Fig. 36a (curves 1–3, respectively). The dashed line in this figure shows the development of a resonance (which can be extremely undesirable) as the inductance L_0 is increased or the input resistance of the amplifier R is decreased.

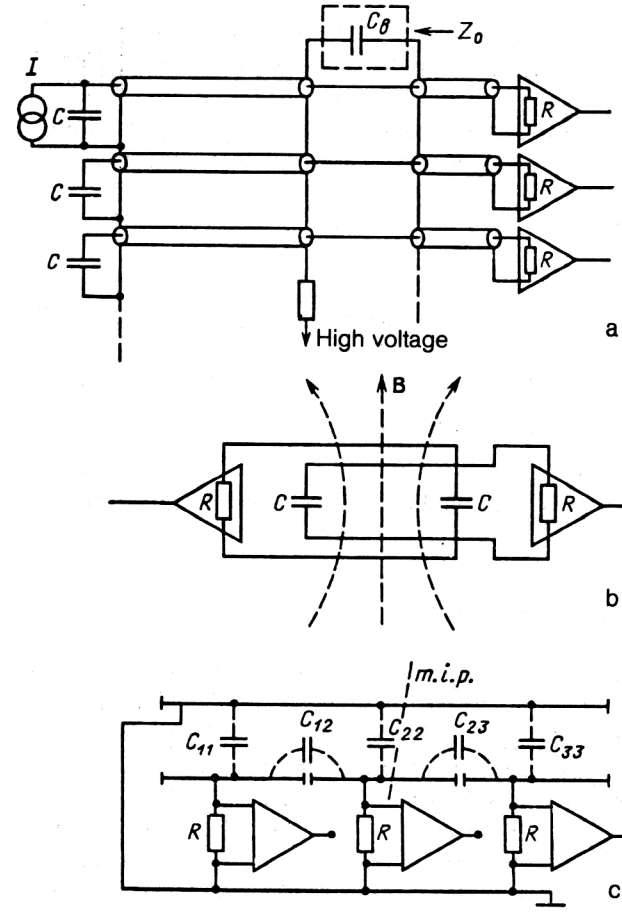

FIG. 34. Development of cross-talk in neighboring channels: (a) voltage drop at the common impedance Z_0; (b) common magnetic flux (inductive coupling); (c) parasitic capacitive coupling (C_{12}) and induction effect.

2. Inductive coupling between channels

This arises when two (or several) channels are penetrated by a common magnetic flux inducing an emf in a channel where there is no energy release by particles (Fig. 34b). The method of suppression is obvious—decrease of the loop areas and correct orientation in space, and the use of coaxial cables for connections. The latter method has a number of deficiencies.

The cable capacitance can be comparable with, or even larger than, the capacitance of an individual chamber, which tends to increase the electronics-noise contribution; isolation of the cable can contaminate the working medium by electronegative admixtures (a high degree of purity is required in a number of applications, for example, for the Time–Projection Chamber).

The equivalent circuit for analyzing pickup is given in Fig. 35b. The equation for the loop currents in operator form is

$$Z_1 i_1 + pMi_2 = I/(pC), \tag{134}$$

$$Z_2 i_2 + pMi_1 = 0, \tag{135}$$

where I is the current in the detector, C is the detector capacitance, and $Z_{1,2}$ are the total impedances of the loops,

$$Z_{1,2} = Z = pL + R + 1/(pC),$$

$L_{1,2} = L$ are the loop inductances, $M = k\sqrt{(L_1 L_2)}$ is the mutual inductance, and k is the magnetic-coupling coefficient.

The ratio of the currents i_1 and i_2 gives the transfer function of the cross-talk at a neighboring channel:

$$K_I(p) = \frac{i_2}{i_1} = \frac{p^2 MC}{p^2 LC + pRC + 1} = k\frac{p^2}{p^2 + pR/L + 1/(LC)}. \tag{136}$$

For strong damping $4L \ll R^2 C$ of the pole (136) we have

$$p_1 = -1/(RC); \quad p_2 = -R/L,$$

but for $4L_1 > R^2 C$ a resonance appears. The Bode diagrams of the cross-talk transfer functions are shown in Fig. 36b.

3. The induction effect

In this case the electromagnetic field of the drift electrons induces a current directly in several neighboring electrodes. The effect is the greater, the larger the ratio of the cathode–anode gap to the electrode width, and the smaller, the smaller the drift length of the electrons. This effect can prove useful—in Ref. 64 it was shown that it is possible to reconstruct the coordinates of a particle track by analyzing the form of the induced currents. However, it can also lead to errors, for example, in those cases where the electron (photon) coordinate is reconstructed from the ratio of the charges in neighboring chambers. In practice, the induction effect appears not in a pure form, but in conjunction with interference capacitance.

4. The capacitance effect

This arises from the presence of nonzero amplifier resistance. Because of this, when a current passes through one chamber, the potential of its anode (cathode) changes, and via capacitive coupling to neighboring electrodes it induces a signal in them. In Fig. 34c we illustrate the development of inductive and capacitive interference in the case of an ionization chamber with planar electrode geometry when a minimally ionizing particle (m.i.p.) passes through it, and in Fig. 35c we show the equivalent circuit for calculating interference of this type in the case where the particle induces a current only in the three central electrodes (large electrode width–gap ratio). Then, following Refs. 65 and 66, for these conductors we can write down a system of equations coupling the induced currents I_i $(i = 1,2,3)$ to the currents i_i $(i = 1,2,3)$ flowing to the external circuit of the electrodes:

$$\left.\begin{aligned} I_1 &= \beta_{11}\frac{dU_1}{dt} + \beta_{21}\frac{dU_2}{dt} + i_1, \\ I_2 &= \beta_{12}\frac{dU_1}{dt} + \beta_{22}\frac{dU_2}{dt} + \beta_{23}\frac{dU_3}{dt} + i_2, \\ I_3 &= \beta_{23}\frac{dU_2}{dt} + \beta_{33}\frac{dU_3}{dt} + i_3, \end{aligned}\right\} \tag{137}$$

where U_i $(i = 1,2,3)$ is the voltage drop at the input impedances of the amplifiers and β_{ik} are the capacitive coefficients.

A technique for calculating the induction currents for calorimeters with planar electrode geometry is the following. The density of the distribution of charge $\rho(x)$ induced by a point charge Q located between the infinite conducting electrodes of the chamber is given by[67,68]

$$\rho(x) = \frac{Q}{2d}\frac{\cos(\pi y/d)}{\cosh(\pi x/d) - \sin(\pi y/d)}, \tag{138}$$

where d is the gap between the anode and the cathode, x is the coordinate along the chamber electrodes (the charge Q has $x = 0$), and y is the coordinate of the charge location perpendicular to the electrode plane and measured from the center of the gap between the planes. For a track perpendicular to the plane of the chamber, in the case of complete ionization-electron collection at the anode, when a "column" of positive ions remains in the gap of the chamber, the density of charge drawn to the cathode can be written as

$$\rho(x) = \frac{Q_1}{\pi d}\ln\left[\frac{\cosh(\pi x/d) + 1}{\cosh(\pi x/d) - 1}\right], \tag{139}$$

where Q_1 is the ionic charge of a particle track uncanceled by electrons. Assuming that Q_1 is a function of the time and integrating (139) over the coordinate x between limits determined by the electrode width, it is easy to find the currents induced at the electrodes. In the case of detectors with a more complicated electric field configuration the induction currents can be calculated, for example, using the Ramo–Shockley theorem.[69,70]

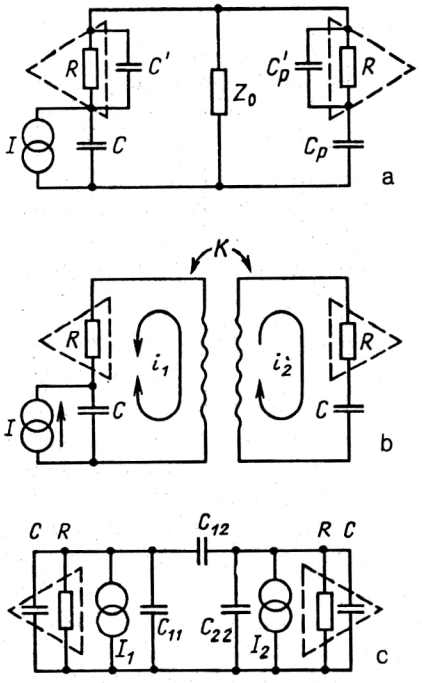

FIG. 35. Equivalent substitution circuits for calculating the pickup transfer function of Figs. 34a–34c, respectively.

In the motion of a point charge relative to a system of grounded conductors, an induced current given by the following expression appears in the circuit of the kth electrode:

$$I_k(t)=Qv\,\mathrm{grad}_{\mathbf{v}}\{\psi_k[x(t),y(t),z(t)]\}, \tag{140}$$

where $\mathbf{v}$ is the velocity of the charge Q, ψ_k is a function satisfying the Laplace equation and taking the value unity at the kth electrode and zero at the others, $\mathrm{grad}_{\mathbf{v}}\{\psi_k\}$ is the projection of the gradient on the direction of the velocity, and $x(t)$, $y(t)$, and $z(t)$ are the coordinates of the point at which the charge Q is located.

Equations (138) and (139) were used to carry out calculations of the currents I_1–I_3 for the geometry of the MARS-2 detector[71] (for which the ratio of the electrode and gap widths is 10 cm/2.8 cm). Two cases were studied—those of pure and dirty ($\varepsilon^{-1}=650$ nsec) argon, and it was assumed that the particle intersects the electrodes perpendicular to their plane. The position of the particle along the x axis was varied. It was shown that the shape of the pulse induced in a neighboring channel is practically independent of x and can be approximated by a parabola in the case of pure argon, and by the function $t\exp(-t\varepsilon)$ in the case of dirty argon. Calculations show that the amplitude of the pulse induced at a neighboring channel depends strongly on the coordinates of the particle trajectory and can be written as

$$A(x)=C_1\exp(C_2x),$$

where $C_{1,2}$ are constants depending on the electrode geometry.

Let us consider the system of equations (137) only for the first and second electrodes (the particle passes through the second). We neglect the terms with the coefficients $\beta_{12,23}$ in the second equation of the system and rewrite (137) as

$$I_1=\beta_{11}\frac{dU_1}{dt}+\beta_{21}\frac{dU_2}{dt}+i_1,$$
$$I_2=\beta_{22}\frac{dU_2}{dt}+i_2. \tag{141}$$

In the case of dirty argon $I_{1,2}$ have the form

$$I_1=A(x)E(\varepsilon t)\exp(-\varepsilon,t); \tag{142}$$

$$I_2=E\exp(-\varepsilon t), \tag{143}$$

where $E=V_d\,dQ/dx$ is the amplitude of the induced current, dQ/dx is the charge density of the track from a minimally ionizing particle, and v_d is the electron drift velocity. The difference between the equivalent circuit of Fig. 35c and that given in Ref. 72 is the presence of the source of a second current I_2 depending on the coordinates of the particle trajectory (I_1 is the signal from a particle at the electrode through which the particle has passed). The currents $i_{1,2}$ and voltages $U_{1,2}$ are related by the imput impedance of the preamplifier:

$$U_{1,2}=i_{1,2}R(1+pRC')^{-1}=i_{1,2}[C'(p+\alpha_{\text{in}})]^{-1}, \tag{144}$$

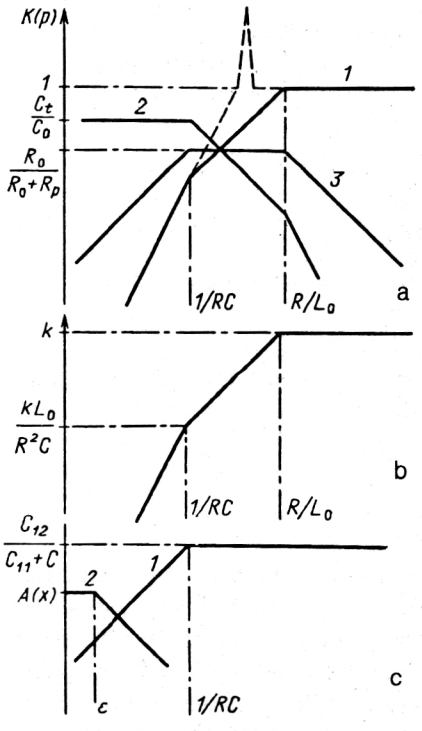

FIG. 36. Bode diagrams of the pickup transfer characteristics: (a) on the common impedance Z_0; curve *1* corresponds to the case $Z_0=pL_0$, *2* to the case $Z_0=pL_0+(pC_0)^{-1}$, *3* to the case $Z_0=pL_0+r_0$; (b) for inductive coupling between channels; L_0 is the inductance of conductors generating a common magnetic flux, k is the flux-coupling coefficient; (c) owing to the parasitic capacitance C_{12} between detector channels (curve 1) and to the induction effect (curve 2); ε^{-1} is the characteristic duration of the particle-induced signal.

where $C' = C + C_{11} = C + C_{22}$, C is the input capacitance of the preamplifier, and $\alpha_{in} = 1/(RC')$.

Performing the Laplace transform (141), taking into account Eqs. (142)–(144), we obtain

$$U_2(p) = \frac{E}{C'} \frac{1}{p+\varepsilon} \frac{1}{p+\alpha_{in}}, \tag{145}$$

$$U_1(p) = \gamma \frac{E/C'p}{(p+\varepsilon)(p+\alpha_{in})^2} + A(x) \frac{E}{C'} \frac{\varepsilon}{(p+\varepsilon)^2(p+\alpha_{in})}, \tag{146}$$

where $\gamma = C_{12}/C' = C_{12}/(C + C_{11})$.

The transfer characteristic of the interference appearing in a neighboring electrode has the form

$$K_U(p) = \frac{U_1(p)}{U_2(p)} = \gamma \frac{p}{p+\alpha_{in}} + A(x) \frac{\varepsilon}{p+\varepsilon}. \tag{147}$$

For frequencies $\omega > \alpha_{in}$ the first term in the last expression gives the derivative of the signal, as was noticed in Ref. 72. The second term in (147) has a purely inductive nature, so that it depends on the point of intersection of the particle and is determined by the specific geometry of the ionization chamber.

It follows from Eq. (147) that the capacitive pickup is proportional to the partial capacitance C_{12} and the resistance of the amplifier, and the inductive pickup is independent of the impedance. The Bode diagram of the pickup transfer function is shown in Fig. 36c.

[1)]FWHM is the full width at half the maximum of the spectrum.

[1] P. F. Manfredi and F. Ragusa, Nucl. Instrum. Methods **A235**, 345 (1985).
[2] P. F. Manfredi, Fiz. Elem. Chastits At. Yadra **15**, 982 (1984) [Sov. J. Part. Nucl. **15**, 439 (1984)].
[3] Yu. K. Akimov, O. V. Ignat'ev, A. I. Kalinin, and V. F. Kushniruk, *Semiconductor Detectors in Experimental Physics* [in Russian] (Énergoatomizdat, Moscow, 1989).
[4] A. Litke, C. Adolphsen, A. S. Schwarz *et al.*, Nucl. Instrum. Methods **A265**, 93 (1988).
[5] W. Buttler, B. J. Hosticka, G. Lutz, and G. Zimmer, Nucl. Instrum. Methods **A253**, 439 (1987).
[6] J. K. Millard, T. V. Blalock, and N. W. Hill, IEEE Trans. Nucl. Sci. **NS-19**, 388 (1972).
[7] G. P. Avondo, P. D'Angelo, P. Jarron *et al.*, Nucl. Instrum. Methods **A241**, 107 (1985).
[8] V. Radeka, IEEE Trans. Nucl. Sci. **NS-21**, 51 (1974).
[9] E. Gatti and P. F. Manfredi, IEEE Trans. Nucl. Sci. **NS-25**, 66 (1978).
[10] N. Karlovac and T. Mayhugh, IEEE Trans. Nucl. Sci. **NS-24**, 327 (1977).
[11] R. N. Krasnokutskiĭ, N. N. Fedyakin, and R. S. Shuvalov, Preprint 86-37, IHEP, Serpukhov (1986) [in Russian].
[12] P. Rehak, *Detectors and Signal Processing for High Energy Physics*, BNL 30214 OG599, Brookhaven National Laboratory, NY (1981).
[13] M. Bertolaccini, G. Padovini, D. V. Camin *et al.*, Nucl. Instrum. Methods **A264**, 399 (1988).
[14] R. N. Krasnokutskiĭ, L. L. Kurchaninov, V. V. Tikhonov *et al.*, Preprint 89-132, IHEP, Serpukhov (1989) [in Russian].
[15] R. N. Krasnokutskiĭ, L. L. Kurchaninov, V. V. Tikhonov *et al.*, Prib. Tekh. Eksp. No. 6, 111 (1986) [Instrum. Exp. Tech. (USSR)].
[16] R. N. Krasnokutskiĭ, L. L. Kurchaninov, V. V. Tikhonov *et al.*, Prib. Tekh. Eksp. No. 1, 140 (1989) [Instrum. Exp. Tech. (USSR)].
[17] R. N. Krasnokutskiĭ, L. L. Kurchaninov, V. V. Tikhonov *et al.*, Prib. Tekh. Eksp. No. 3, 129 (1988) [Instrum. Exp. Tech. (USSR)].
[18] R. N. Krasnokutskiĭ, L. L. Kurchaninov, V. V. Tikhonov *et al.*, Preprint 88-116, IHEP, Serpukhov (1988) [in Russian].
[19] R. N. Krasnokutskiĭ, L. L. Kurchaninov, V. V. Tikhonov *et al.*, Preprint 89-49, IHEP, Serpukhov (1989) [in Russian].
[20] É. Stolyarskiĭ, *Measurement of Transistor Parameters* [in Russian] (Sov. Radio, Moscow, 1976).
[21] *Transistors. Parameters, Measuring and Testing Methods* [in Russian], edited by I. G. Bergel'son, Yu. A. Kamenetskiĭ, and I. F. Nikolaevskiĭ (Sov. Radio, Moscow, 1968).
[22] L. L. Kurchaninov, V. V. Tikhonov, and R. S. Shuvalov, Prib. Tekh. Eksp. No. 1, 142 (1988) [Instrum. Exp. Tech. (USSR)].
[23] R. N. Krasnokutskiĭ, L. L. Kurchaninov, V. V. Tikhonov *et al.*, Prib. Tekh. Eksp. No. 5, 118 (1988) [Instrum. Exp. Tech. (USSR)].
[24] *Semiconductor Devices: Transistors. Handbook* [in Russian], edited by N. N. Goryunov (Énergoatomizdat, Moscow, 1986).
[25] E. Hejne and P. Jarron, IEEE Trans. Nucl. Sci. **NS-29**, 405 (1982).
[26] P. D'Angelo, A. T. Hrisoho, and P. Jarron, Nucl. Instrum. Methods **193**, 533 (1982).
[27] R. N. Krasnokutskiĭ, L. L. Kurchaninov, V. V. Tikhonov *et al.*, Preprint 88-196, IHEP, Serpukhov (1988) [in Russian].
[28] P. Jarron and M. Goyot, Nucl. Instrum. Methods **226**, 156 (1984).
[29] V. G. Ivochkin, R. N. Krasnokutskiĭ, L. L. Kurchaninov *et al.*, Preprint 86-229, IHEP, Serpukhov (1986) [in Russian].
[30] R. N. Krasnokutskiĭ, L. L. Kurchaninov, V. V. Tikhonov *et al.*, Preprint 89-206, IHEP, Serpukhov (1989) [in Russian].
[31] V. M. Golovin, R. N. Krasnokutskiĭ, L. L. Kurchaninov *et al.*, Preprint 89-231, IHEP, Serpukhov (1989) [in Russian].
[32] R. N. Krasnokutskiĭ, Yu. M. Pishchal'nikov, and R. S. Shuvalov, Preprint 83-142, IHEP, Serpukhov (1983) [in Russian].
[33] R. A. Boie, A. T. Hrisoho, and P. Rehak, IEEE Trans. Nucl. Sci. **NS-28**, 603 (1981).
[34] J. Fischer, A. T. Hrisoho, V. Radeka, and P. Rehak, Nucl. Instrum. Methods **A238**, 249 (1985).
[35] P. P. Kostromin, R. N. Krasnokutskiĭ, L. L. Kurchaninov *et al.*, Prib. Tekh. Eksp. No. 6, 40 (1988) [Instrum. Exp. Tech. (USSR)].
[36] L. L. Kurchaninov, V. K. Myalitsyn, V. V. Sushkov, and R. S. Shuvalov, Preprint 89-131, IHEP, Serpukhov (1989) [in Russian].
[37] E. N. Gushchin, L. L. Kurchaninov, Yu. V. Musienko *et al.*, Preprint 89-232, IHEP, Serpukhov (1989) [in Russian].
[38] R. Henderson, W. Faszer, R. Opeskaw *et al.*, Preprint TRI-PP-88-97, Vancouver (1988).
[39] V. Radeka and N. Karlovac, Nucl. Instrum. Methods **52**, 86 (1967).
[40] M. Conrad, IEEE Trans. Nucl. Sci. **NS-15**, 268 (1968).
[41] V. Radeka, IEEE Trans. Nucl. Sci. **NS-15**, 455 (1968).
[42] F. S. Goulding, Nucl. Instrum. Methods **100**, 493 (1972).
[43] M. O. Deighton, Nucl. Instrum. Methods **58**, 201 (1968).
[44] F. S. Goulding and D. A. Landis, IEEE Trans. Nucl. Sci. **NS-29**, 1125 (1982).
[45] R. N. Krasnokutskiĭ, L. L. Kurchaninov, V. V. Tikhonov *et al.*, Preprint 89-50, IHEP, Serpukhov (1989) [in Russian]; Nucl. Instrum. Methods **A291**, 634 (1990).
[46] R. N. Krasnokutskiĭ, L. L. Kurchaninov, V. V. Tikhonov *et al.*, Prib. Tekh. Eksp. No. 1, 140 (1989) [Instrum. Exp. Tech. (USSR)].
[47] R. N. Krasnokutskiĭ, L. L. Kurchaninov, V. V. Tikhonov *et al.*, Preprint 89-133, IHEP, Serpukhov (1989) [in Russian].
[48] R. N. Krasnokutskiĭ, L. L. Kurchaninov, V. V. Tikhonov *et al.*, Preprint 89-46, IHEP, Serpukhov (1989) [in Russian]; Nucl. Instrum. Methods **A292**, 450 (1990).
[49] W. J. Willis and V. Radeka, Nucl. Instrum. Methods **120**, 221 (1974).
[50] C. Cerri, S. P. Denisov, G. Gennaro *et al.*, Nucl. Instrum. Methods **214**, 217 (1983).
[51] R. L. Chase, C. H. Gruhn, A. Hrisoho *et al.*, in *Proc. of the Second ISPRA Nuclear Electronics Symposium*, 1975, p. 29.
[52] V. Radeka, *Calorimeter Notes*, BNL Report, Brookhaven National Laboratory, September 1973.
[53] E. Gatti and P. F. Manfredi, Nucl. Instrum. Methods **226**, 142 (1984).
[54] E. Gatti, P. F. Manfredi, and D. Marioli, Nucl. Instrum. Methods **193**, 539 (1982).
[55] E. Gatti and P. F. Manfredi, Riv. Nuovo Cimento **9**, No. 1 (1986).
[56] R. N. Krasnokutskiĭ, N. N. Fedyakin, and R. S. Shuvalov, Preprint 86-9, IHEP, Serpukhov (1986) [in Russian].
[57] R. N. Krasnokutskiĭ, N. N. Fedyakin, and R. S. Shuvalov, Preprint 86-33, IHEP, Serpukhov (1986) [in Russian].
[58] R. N. Krasnokutskiĭ, N. N. Fedyakin, and R. S. Shuvalov, Preprint

86-199, IHEP, Serpukhov (1986) [in Russian].
[59] R. N. Krasnokutskiĭ, N. N. Fedyakin, and R. S. Shuvalov, Preprint 87-108, IHEP, Serpukhov (1987) [in Russian].
[60] H. B. Callen and T. A. Welton, Phys. Rev. **83**, 34 (1951).
[61] L. D. Landau and E. M. Lifshitz, *Electrodynamics of Continuous Media*, transl. of 2nd Russ. ed. (Pergamon Press, Oxford, 1984) [Russ. original, 3rd ed., Nauka, Moscow, 1991].
[62] M. L. Levin and S. M. Rytov, *Theory of Equilibrium Thermal Fluctuations in Electrodynamics* [in Russian] (Nauka, Moscow, 1967).
[63] E. Gatti, P. F. Manfredi, and G. Ripamonti, Nucl. Instrum. Methods **A257**, 331 (1987).
[64] V. I. Balbekov, A. M. Baranov, R. N. Krasnokutsky *et al.*, Preprint 79-125, IHEP, Serpukhov (1979).
[65] V. P. Pronin and L. A. Shekhtman, Zh. Tekh. Fiz. **37**, 1387 (1967) [Sov. Phys. Tech. Phys. **12**, 1007 (1968)].
[66] R. N. Krasnokutskiĭ, L. L. Kurchaninov, V. V. Tikhonov *et al.*, Preprint 89-48, IHEP, Serpukhov (1989) [in Russian]; Nucl. Instrum. Methods **A292**, 445 (1990).
[67] E. Mathieson and J. S. Gordon, Nucl. Instrum. Methods **227**, 267 (1984).
[68] P. K. Lebedev, A. V. Maksimov, S. V. Murav'ev, and G. V. Fedotovich, Preprint FIAN-63, Lebedev Institute, Moscow (1989) [in Russian].
[69] W. Shockley, J. Appl. Phys. **9**, 635 (1938).
[70] S. Ramo, Proc. IRE **27**, 584 (1939).
[71] C. Cerri, S. P. Denisov, G. Gennaro *et al.*, Nucl. Instrum. Methods **227**, 227 (1984).
[72] R. L. Chase and J. P. Richer, IEEE Trans. Nucl. Sci. **NS-31**, 258 (1984).

Translated by Patricia Millard